The Effect of the Distribution of Cu and Ag in Tandem Catalysts on the Production of Ethylene in the Electrocatalytic CO_2 Reduction Reaction

Master's Thesis by Alexander P. Flick

Supervision by:

Prof. dr. P.E. De Jongh

Dr. P. Ngene

F. Mattarozzi

April 16, 2023

Abstract

The increasing demand for electrical energy storage due to the energy transition has prompted research into the electrocatalytic reduction of CO_2. Concentrating on the production of ethylene is a promising approach to increase the cost-efficiency and feasibility of the process. Cu-based catalysts can convert CO_2 into ethylene, but the poor activity of Cu alone for the first step reduction of CO_2 into *CO puts limitations on the production of ethylene. Tandem catalysis divides the reaction pathway towards ethylene into two segments, with silver being an excellent metal for the first segment that reduces CO_2 to CO and Cu facilitating the second segment where *CO is reduced to ethylene. Utilizing this concept, the effective transfer of CO from Ag to Cu active sites is essential to steer the CO_2RR toward the production of ethylene. This study prepared and tested several Cu-Ag catalysts with different distributions of Cu and Ag, using electrodeposition, co-deposition, and galvanic replacement, and evaluated their effectiveness of synergy (i.e., transfer of CO from Ag to Cu active sites based on the product ratio of ethylene and CO. The results showed that interfacial contact enhanced the effectiveness of synergy compared to separated metals. Furthermore, the homogeneous distribution of Cu and Ag resulted in the relatively high partial current densities and Faradic efficiencies for ethylene and CO. The catalyst prepared by galvanic replacement with a 1 mM $AgNO_3$ solution for 2 minutes showed uniquely higher activity and selectivity towards ethylene than CO, resulting in the most effective synergy. Additionally, this study presents a method to synthesize uniform Cu_2O nanospheres of 0.87 µm via polyol synthesis. The galvanic replacement was performed on these particles but exhibited overall very poor catalytic activity and selectivity, favoring the HER. It is suggested that this is related to the use of porous carbon paper as substrate. This is because the majority of the Cu_2O nanospheres remained unaffected by galvanic replacement, exhibiting the poor activity of Cu for the reduction of CO_2.

Layman’s abstract

Currently, an energy transition is taking place to mitigate climate change where it is expected that electrical energy provides a large amount of the global energy demand, but insufficient grid-scale storage limits mass-scale integration. Therefore, a process is developed that can store electrical energy by conversion of carbon dioxide (CO_2) into useful products. One valuable product is ethylene, which can be made from CO_2 using a catalyst composed of copper. However, copper has a poor ability to convert CO_2 alone, which puts limitations on the production of ethylene. Previous research has found that the addition of silver helps to improve the ability of copper to convert CO_2. Because the metals must work together to produce ethylene, the distribution of Cu and Ag is very important in the catalyst. In this study, different ways of putting copper and silver together were used. Then, the cooperation of the metals was measured during CO_2 conversion. It was found that interfacial contact between the metals is necessary to improve the cooperation of the metals and the best cooperation was obtained when copper was coated with a thin layer of silver. If we can figure out how to create this cooperation between Cu and Ag on a larger scale to efficiently produce ethylene, this process could be a cost-effective and feasible way to store electrical energy.

List of abbreviations

CO_2	Carbon dioxide
CO_2RR	Electrocatalytic CO_2 Reduction Reaction
HER	Hydrogen evolution reaction
Cu	Copper
Ag	Silver
*	Bound reaction intermediate
$FE_{product}$	Faradaic efficiency towards product
SHE	Standard hydrogen electrode
RHE	Reversible hydrogen electrode
Cu_2O	Copper(I) oxide
OER	Oxygen evolution reaction
E^0	Standard reduction potential
Ag/AgCl	Silver chloride electrode
$KHCO_3$	Potassium bicarbonate
Ar	Argon
CO	Carbon monoxide
HCOOH	Formic acid
CH_4	Methane
C_2H_4	Ethylene
C_2H_5OH	Ethanol
PCET	Proton-coupled electron transfer
Cu^{2+}	Copper(II)
Cu^{+}	Copper(I)
Ag^{+}	Silver(I)

GC	Gas chromatography
NMR	Nuclear magnetic resonance spectroscopy
XRD	X-ray diffraction
SEM	Scanning electron microscopy
EDX	Energy dispersive X-ray spectroscopy
TEM	Transmission electron microscopy

Table of contents

Chapter I

Introduction

The transition to fossil fuel economy began around 1750 when the steam engine was developed.[1] Since then, the use of fossil fuels as a primary energy source has been affecting Earth's climate through emissions of greenhouse gases. The global average surface temperature has risen to nearly 1.2 ˚C above pre-industrial levels and is projected to be at the 1.5 ˚C level within 20 years. The United Nations Intergovernmental Panel on Climate Change warned that exceeding a 1.5 ˚C temperature increase will have a dramatic impact on human societies and ecosystems, resulting in droughts, rising sea levels, unprecedented floods, heat waves, and famine. The temperature increase can be limited to 1.5 ˚C if CO_2 emissions are reduced by 45% over 2010 levels by 2030, and net zero carbon emissions are achieved by 2050.[2]

To mitigate the effects of CO_2 emissions, technologies are being developed with low-carbon, zero-carbon, and even negative-carbon footprints. These technologies are crucial not only for enabling net zero carbon emissions but also for potentially reversing global warming by removing excess CO_2 from the atmosphere.[2] The transition towards green renewable energy holds great potential to replace fossil fuels in significant amounts. The electricity generated from wind and solar power has already provided for 10.2% of global energy in 2021.[1,3] Due to their intermittent nature, a satisfactory storage capacity of electricity is essential to provide energy during periods of low wind and cloud cover. However, mass-scale integration of electrical energy is not yet feasible due to insufficient grid-scale storage. Despite progress being made, projected growth in grid-scale storage capacity is not keeping pace to achieve net zero carbon emissions by 2050.[4,5] Therefore, technologies are developed that enable the storage of electricity in chemical processes.

The electrocatalytic CO_2 reduction reaction (CO_2RR) is an emerging technology that involves the electrochemical conversion of CO_2 to hydrocarbons and oxygenates such as carbon monoxide, formic acid, methane, ethylene, ethanol, and n-propanol. The reduction of water in the hydrogen evolution reaction (HER) competes with the CO_2RR and reduces the energy efficiency of the process, hence it is desirable to suppress this reaction. Nevertheless, the rational design of electrocatalysts is still facing a significant challenge to suppress the HER. Another challenge to overcome is that in practice an additional potential above the thermodynamically determined reduction potential must be applied to drive the reduction of CO_2. These overpotentials should be kept as low as possible to increase the energy efficiency of the technology.[6]

Despite these challenges, the technology holds great promise for the storage of electrical energy through the conversion of CO_2 into a wide range of products with significant global demand and market value.[4] The practical feasibility could be greatly improved by concentrating on the production of ethylene in the CO_2RR, which is a vital component in consumer plastics and is produced at an annual rate of approximately 150 million metric tons.[7] Traditional production is done by steam cracking of naphtha, while newer methods such as catalytic dehydrogenation of

light alkanes or Fischer-Tropsch synthesis also rely on fossil fuels.[8] Hence, the CO_2RR could provide an environmentally friendly and sustainable alternative to decrease the dependence on fossil fuels in ethylene production. Based on the work of Hori et al.[9], the active metals are divided into four groups with products hydrogen, formate, CO, or beyond *CO. For instance, silver and zinc produce CO (g), while platinum promotes the HER. Copper (Cu) is the only metal that belongs to the group beyond *CO because it can retain *CO at its surface allowing further reduction to occur.[10] This unique property opens doors for commercializing the CO_2RR through the production of ethylene. However, the limited activity of Cu to reduce CO_2 into *CO during the first step restricts the activity and selectivity of the CO_2RR. It is suggested that the primary reaction pathway to ethylene involves *CO dimerization, by which increasing the abundance of *CO as a key intermediate is an interesting approach to promote this mechanism.[11,12] Previous studies showed that there are several methods to steer the CO_2RR towards ethylene in Cu-based catalysts through oxide[13] and halide-derived Cu nanoparticles[14], facet-dependent Cu nanostructures[15], functionalized Cu nanoparticles[16], and bimetallic Cu systems[17].

Employing a tandem strategy to divide the reaction pathway to ethylene into segments is an interesting approach to overcome the limited activity of Cu. In the first segment, independent active sites are responsible for the reduction of CO_2 into CO, and in the second segment *CO is reduced by Cu. This synergistic mechanism involves the transfer of CO between the independent active sites, and the effectiveness of this transfer influences the catalytic selectivity and activity of the CO_2RR towards ethylene. For instance, the study of Huang et al.[17] showed the Cu-Ag interface in nanodimers resulted in a 3.4-fold enhancement in $FE_{ethylene}$ and a 2-fold improvement in the total current density at -1.1 V vs RHE compared to Cu nanoparticles of similar size and shape. Another study by Chen et al.[18] achieved a 4-fold enhancement of multi-carbon product conversion with a $Cu_{500}Ag_{1000}$ catalyst without mutual electronic interaction between the two metals. Silver (Ag) is known as the most active and selective catalyst for CO_2RR towards CO. To optimize the catalytic activity and selectivity of tandem catalysts towards ethylene, it is essential to achieve the most effective transfer of CO between Cu and Ag. Consequently, the energy efficiency of the technology can be improved, increasing its potential to be implemented as a cost-effective carbon-utilizing and energy-storing process.

To study the effectiveness of synergy (i.e., CO transfer), several catalysts with different distributions of Cu and Ag sites are prepared using electrodeposition, co-deposition, and galvanic replacement. The catalysts are tested to study their activity and selectivity for CO_2RR products. Based on the relative production of CO and ethylene, the effectiveness of CO transfer can be assessed. Subsequently, the distribution of Cu and Ag sites resulting in the most effective transfer of CO is applied to prepare Cu_2O-Ag nanospheres to further improve the catalytic activity and selectivity. The work of da Silva et al.[19] showed that a $FE_{ethylene}$ of 20% was achieved for oxide-derived Cu nanospheres. The preparation of uniform Cu_2O nanospheres was performed using a polyol synthesis.[20]

Chapter II

Theory

2.1 Redox chemistry

A redox reaction consists of a reduction and oxidation reaction in which the electrons are accepted and donated by the reactants, respectively. In an electrochemical cell, the reduction process occurs at the cathode or working electrode, while oxidation reactions happen at the anode or counter electrode. The overall reaction is driven by the difference in reduction potential of the two half-reactions, which determines the spontaneity of the reaction through the Gibbs free energy:

$$\Delta G^0 = -nFE^0{}_{cell} \qquad (1)$$

Where:

$$E^0{}_{cell} = E^0{}_{cathode} - E^0{}_{anode} \qquad (2)$$

The reduction potential for processes under standard conditions is given by E^0, which implies unity activity for all electrochemical species involved, T = 298 K, and pressure of 1 atm. The more negative the reduction potential of a half-reaction, the stronger the reducing power of a species. Conversely, the more positive the reduction potential of a half-reaction, the stronger the oxidizing power of a species. The reduction potential under non-standard conditions can be calculated from the Nernst equation:

$$E_{cell} = E^0{}_{cell} - \frac{RT}{nF} \times ln\,(Q) \qquad (Nernst\ equation)$$

Where R is the gas constant = 8.314 J/(K·mol), T is the temperature in K, n is the number of electrons transferred in the redox reaction, F is the Faraday constant = 96485 C/mol and Q is the ratio of the activity between products and reactants. In practice, the electrode potential of a redox process is shifted, because additional energy is required to drive the reaction. This shift is defined as overpotential and is caused by reaction conditions, catalyst properties, and the nature of the reactants and products.[21]

2.2 Electrocatalytic CO_2 reduction reaction

CO_2RR is typically facilitated in an H-type cell. This is an electrochemical cell where the working and counter electrode are isolated in two half-cells allowing reduction and oxidation reactions to occur independently. The electrodes are immersed in a liquid electrolyte, and CO_2 molecules solubilize in the electrolyte and diffuse down a concentration gradient to the cathode. As a result, CO_2RR can be described by the following cathodic reaction:

$$x\mathrm{CO_2} + n\mathrm{H^+} + n\mathrm{e^-} \rightarrow \mathrm{product} + y\mathrm{H_2O} \qquad (CO_2RR)$$

CO_2 is a very stable molecule with two linear C=O bonds characterized by high bonding energy of 750 kJ·mol^{-1} each. Consequently, CO_2 reduction reactions are non-spontaneous, and an electrolyzer is needed to split water at the counter electrode using electrical energy to provide protons and electrons. This process is known as the oxygen evolution reaction:

$$2\mathrm{H_2O\ (l)} \rightarrow 4\mathrm{H^+} + 4\mathrm{e^-} + \mathrm{O_2(g)} \qquad E^0{}_{\mathrm{RHE}} = 1.23 \qquad (OER)$$

Water is a renewable and scalable source of electrons and protons and therefore commonly implemented as a medium for electrolytes. However, catalytic activity is restricted by mass transport limitations due to the poor solubility and slow diffusion of CO_2 in water. This phenomenon is alleviated in flow cells with gas-diffusion electrodes, which can achieve current densities of >200 mA cm^{-2}.[22] Nevertheless, H-cells with aqueous electrolytes are still very suitable for evaluating the CO_2RR at low current densities. In Table 1 the most commonly reported products are summarized with their standard reduction potentials, where CO_2 is considered a gas and water a liquid.[4,23] Suppression of the reduction of water is challenging because the reduction potentials used to drive CO_2RR are in a similar range as the hydrogen evolution reaction:

$$2\mathrm{H_2O(l)} + 2\mathrm{e^-} \rightarrow \mathrm{H_2(g)} + 2\mathrm{OH^-} \qquad E^0{}_{\mathrm{RHE}} = 0 \qquad (HER)$$

Figure 1 depicts the customized H-type cell used for catalytic testing, which is equipped with a potentiostat. The electrolyte (D) of the cathodic half-cell is saturated with CO_2, which diffuses to the catalytic surface of the working electrode (A). The counter electrode (C) in the anodic half-cell should function as an electrolyzer. Commonly used metals are platinum, iridium, and ruthenium.[24] The electrons are flowing from the counter electrode to the working electrode, while the protons can diffuse to the cathodic half-cell through a proton exchange membrane (E). The electrolyte contains dissolved potassium bicarbonate to provide electrical conductivity through the movement of ions.[25] Furthermore, the solution functions as a proton source by buffering the pH, as described by the following equation:

$$\mathrm{CO_2(g)} + \mathrm{H_2O(l)} \leftrightarrow \mathrm{H_2CO_3(l)} \leftrightarrow \mathrm{H^+} + \mathrm{HCO_3{}^-(aq)} \qquad (3)$$

Table 1. Possible Electrocatalytic CO_2 Reduction Reactions with Standard Reduction Potentials

Reduction reaction	E^0 **[V vs RHE]**	**Product name**
$CO_2 + 2H^+ + 2e^- \rightarrow HCOOH(aq)$	-0.12	Formic acid
$CO_2 + 2H^+ + 2e^- \rightarrow CO(g) + H_2O$	-0.10	Carbon monoxide
$CO_2 + 6H^+ + 6e^- \rightarrow CH_3OH(aq) + H_2O$	0.03	Methanol
$CO_2 + 8H^+ + 8e^- \rightarrow CH_4(g) + 2H_2O$	0.17	Methane
$2CO_2 + 8H^+ + 8e^- \rightarrow CH_3COOH(aq) + 2H_2O$	0.11	Acetic acid
$2CO_2 + 10H^+ + 10e^- \rightarrow CH_3CHO(aq) + 3H_2O$	0.06	Acetaldehyde
$2CO_2 + 12H^+ + 12e^- \rightarrow C_2H_5OH(g) + 3H_2O$	0.09	Ethanol
$2CO_2 + 12H^+ + 12e^- \rightarrow C_2H_4(g) + 4H_2O$	0.08	Ethylene
$2CO_2 + 14H^+ + 14e^- \rightarrow C_2H_6(g) + 4H_2O$	0.14	Ethane
$3CO_2 + 18H^+ + 18e^- \rightarrow C_3H_7OH(aq) + 5H_2O$	0.10	Propanol

A reference electrode (B) is added to provide a constant and well-defined potential at the working electrode. In an electrochemical cell, two half-reactions are involved meaning that only the difference between the reduction potentials can be measured, rather than the absolute values. Consequently, a reduction potential is defined relative to the reference electrode, which is typically the standard hydrogen electrode (SHE) or reversible hydrogen electrode (RHE). The reaction of the SHE is defined with a standard electrode potential of 0.00 V:

$$2H^+(aq) + 2e^- \rightleftharpoons 2H_2(g) \qquad E^0{}_{SHE} = 0.00\ V \qquad (SHE)$$

The RHE can be calculated to account for the influence of the pH of the electrolyte on the reduction potential. This relation is derived from the Nernst equation assuming a temperature of 298 K and a hydrogen partial pressure of 1 atm:

$$E_{RHE} = E^0{}_{SHE} - \frac{0.059}{n} \times pH \qquad (Nernst\ equation)$$

Where n is the number of electrons transferred in the redox reaction. In practice, the application of hydrogen-based reference electrodes is complicated due to the requirement of hydrogen gas. To avoid this, a 3 molar Ag/AgCl electrode is used as a reference electrode during catalytic testing.

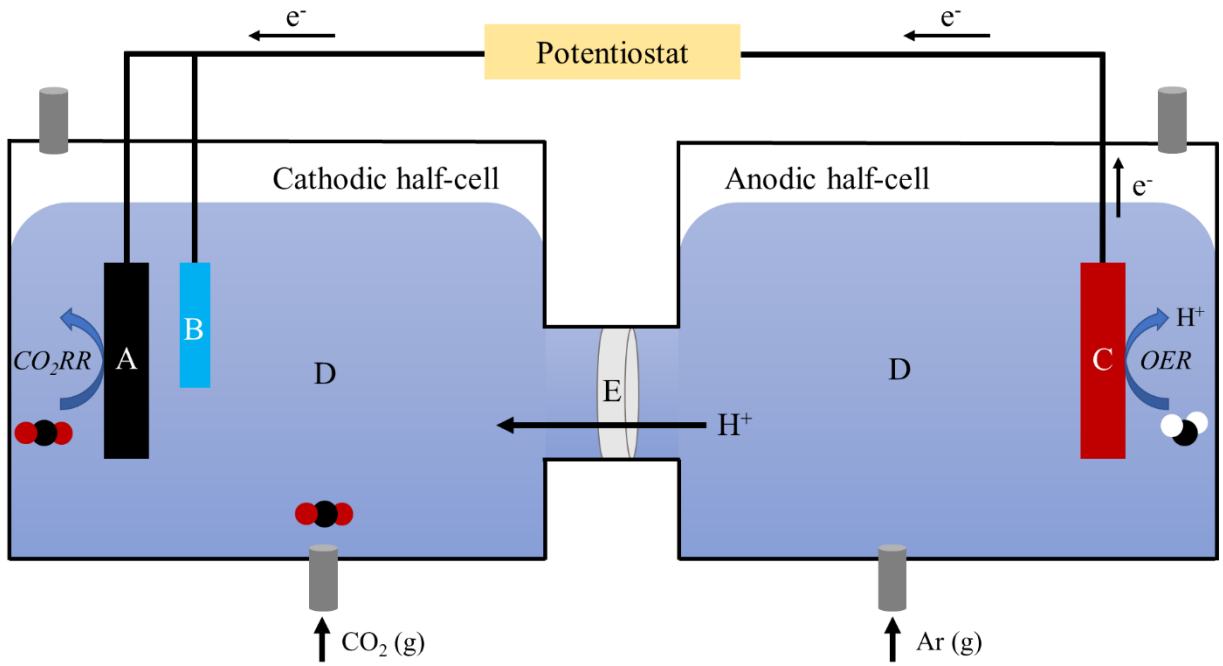

Figure 1. Illustration of the customized H-type cell equipped with a potentiostat. Black, red, and white spheres refer to carbon, oxygen, and hydrogen, respectively. A = cathode or working electrode, B = reference electrode, C = anode or counter electrode, D = electrolyte, and E = proton exchange membrane.

The CO_2RR products are either in the gas phase or dissolved in the electrolyte. The gaseous products are captured by a gas outlet connected to a gas chromatogram, which allows us to directly analyze the products. The liquid products are analyzed by nuclear magnetic resonance spectroscopy. Inert argon gas is bubbled into the electrolyte of the anodic half-cell to equalize the pressure in the half-cells. The catalytic selectivity of CO_2RR is influenced by the type of metal that is used at the working electrode. Hori et al.[9] studied active metals for CO_2RR and analyzed their products. Consequently, the metals could be classified into four groups based on their major product. Hence, it must not be assumed that other products are excluded from the selectivity of a metal class. The first group of metals comprising titanium, iron, nickel, gallium, palladium, and platinum exhibit selectivity to hydrogen through the competitive HER. The second group, which includes cadmium, indium, tin, mercury, thallium, and lead, is selective to formic acid (HCOOH). The third group comprises zinc, silver, and gold, which are selective to carbon monoxide (CO). The last group consists only of copper (Cu), which is the only metal capable of further reducing *CO, where the asterisk refers to a binding site of the metal. Consequently, hydrocarbons and related oxygenates can be produced, including methane (CH_4), ethane (C_2H_6) and ethylene (C_2H_4), acetic acid (CH_3COOH), acetaldehyde (CH_3CHO), methanol (CH_3OH), ethanol (C_2H_5OH) and n-propanol (C_3H_7OH). To understand the selectivity of CO_2RR, reaction pathways to the major products and binding energies of metals to intermediates must be considered. While the exact reaction pathways leading to some of the products are not fully understood, there have been numerous proposed mechanisms that share similarities in terms of key intermediates and proton-

coupled electron transfer (PCET) steps. Kortlever et al.[11] proposed a possible reaction pathway to formic acid summarized by the two elemental PCET steps:

1. $* + CO_2 + H^+ + e^- \rightarrow *OCHO$
2. $*OCHO + H^+ + e^- \rightarrow HCOOH\ (l)$

Formic acid is not involved as an intermediate in the reaction pathway to hydrocarbons or related oxygenates because it can not be reduced further.[26] Likewise, a possible reaction pathway to carbon monoxide was proposed, which is summarized by the three elemental steps:

1. $* + CO_2 + H^+ + e^- \rightarrow *COOH$
2. $*COOH + H^+ + e^- \rightarrow *CO + H_2O$
3. $*CO \rightarrow CO\ (g)$

The production of HCOOH (l) and CO (g) can be explained by the binding energies of the metals to the reaction intermediates. Figures 2A and 2B show the binding energies to *OCHO and *COOH as a descriptor for current density to formic acid and CO, respectively, clearly recalling the Sabatier principle. Likewise, Figure 2C represents the binding energy to *CO as a descriptor for the current density to CO_2RR. Too strong binding energy (high negative) inhibits further reduction resulting in low current density to the related product. Likewise, too weak binding energies (high positive) do not allow sufficient adsorption of the intermediate to reduce further resulting in low current density. For instance, silver has been identified as a good catalyst for CO (g) production. This can be attributed to its negative binding energy to *COOH promoting the formation of *CO, and its very weak binding energy to *CO favoring the release of CO (g).

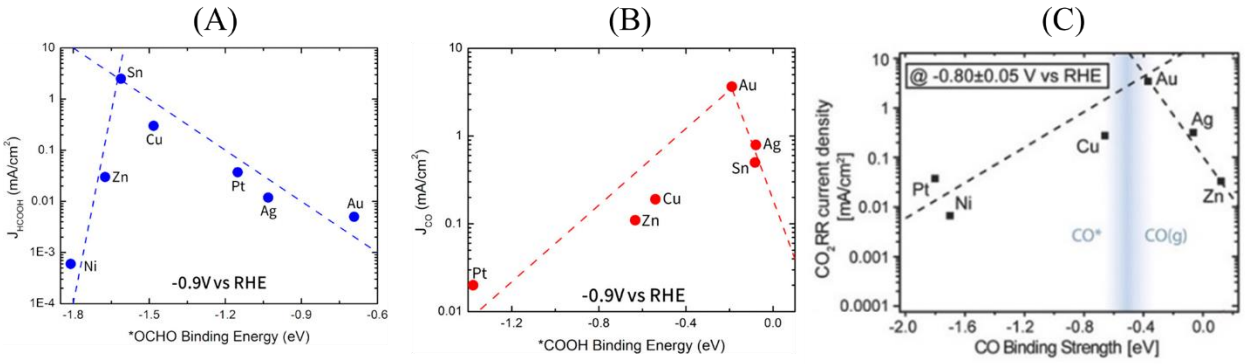

Figure 2. Binding energies to (A) *OCHO, (B) *COOH, and (C) *CO as a descriptor for current density to formic acid, CO, and CO_2RR, respectively.

The reaction pathways to methane and ethylene can be explained using the same approach for Cu. These reaction pathways are described because significant production of methane and ethylene of CO_2RR are observed in this study. Moreover, their mechanisms are very different, with methane begin produced through protonation of *CO, while ethylene can be formed through C-C coupling. A possible mechanism describing the formation of methane was proposed by Kortlever in the four elemental steps:

1. $* + CO_2 + H^+ + e^- \rightarrow *COOH$
2. $*COOH + H^+ + e^- \rightarrow *CO + H_2O$
3. $*CO + H^+ + e^- \rightarrow *COH$
4. $*COH + 5H^+ + 5e^- \rightarrow CH_4$ (g)

It is suggested that the protonation of *CO in step 3 is favored when the abundance of *CO is low leading to the reduction of *CO and subsequent production of methane.[27] Pan et al.[28] proposed a reaction mechanism to ethylene through *CO dimerization, which is summarized by the five elemental steps:

1. $* + CO_2 + H^+ + e^- \rightarrow *COOH$ *(x2)*
2. $*COOH + H^+ + e^- \rightarrow *CO + H_2O$ *(x2)*
3. $*CO + *CO + H^+ + e^- \rightarrow *CO*COH$
4. $*CO*COH + 4H^+ + 4e^- \rightarrow *OCHCH_2 + H_2O$
5. $*OCHCH_2 + 3H^+ + 3e^- \rightarrow C_2H_4$ (g) $+ H_2O$

The ability of Cu to produce and retain *CO on its surface can be attributed to its high binding energy to *COOH and moderate binding energy to *CO. While many studies have suggested various reaction pathways for ethylene production beyond *CO (step 2), the exact mechanism remains unknown.[23,29] Kortlever et al.[11] described *CO dimerization as the primary reaction pathway to ethylene on the Cu(100) crystal plane. Later studies demonstrated that increasing the abundance of *CO at neighboring Cu active sites enhances the catalytic activity and selectivity towards ethylene.[12,30] Even if the formation of ethylene does not necessarily involve *CO dimerization, increasing the surface abundance of *CO on Cu is an effective approach for enhancing the activity and selectivity of CO_2RR towards ethylene.

2.3 Electrodeposition

Electrodeposition or electroplating refers to the deposition of a metallic coating onto a cathodic substrate occurring through the electrochemical reduction of metal ions. The coating is known for its precise thickness, composition, and uniformity. This makes electrodeposition an appropriate technique for the reproducible preparation of metal-based electrodes. As given in Figure 3, the process of electrodeposition is facilitated by the potentiostat.

The cathodic substrate is immersed in a vessel containing the aqueous electrolyte, a reference electrode, and a platinum anode. Typically, the electrolyte consists of a dissolved metal, a complexing agent, and other additives. The reduction of dissolved metal ions can be controlled by complexing agents and additives, which can allow control over the properties of the deposited

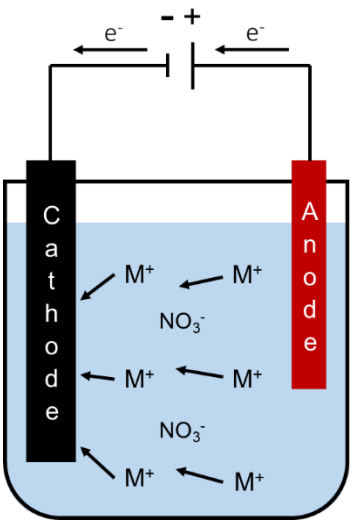

Figure 3. Process of electrodeposition.

material. The deposition of a metal complex is given by the following equation:

$$(M_xL_y)^z + nxe^- \rightarrow xM^0 + yL \qquad (4)$$

$(M_xL_y)^z$ is the complex with oxidation state z, composed of the metal ion M surrounded by the complexing agent L. The mole amounts of M and L are given by *x* and *y*, respectively. The number of electrons needed to reduce one metal ion is given by *n*. Hence, one metal atom is deposited by a charge of *ne* (*e* is the elementary charge of an electron). This enables us to calculate the mass of deposited metal with the utilized charge by the combination of Faraday's Laws of Electrolysis:

$$m = \frac{Q \times M}{n \times F} \qquad (Faraday's\ Law)$$

Where m is the mass of deposited metal, Q is the net charge utilized for electrodeposition in coulombs, M is the molar mass in g/mol, and *n* is the number of electrons transferred to reduce one metal ion. In this study, sodium nitrate was used as an additive for the deposition of Cu, because the competitive reduction of nitrate increases the uniformity of the deposited material. Likewise, ethylenediaminetetraacetic acid was used for the deposition of Ag to prevent dendritic growth, which increases the uniformity of the deposit.[31] A previous study has reported the preparation of homogeneous Cu-Ag coatings with ammonia via co-deposition.[32] During this process, two metals are simultaneously deposited from an electrolyte. Ammonia (NH_3) was added as a complexing agent because it enables the deposition of uniform Cu-Ag coatings through the complexation of copper and silver ions. The reduction of Cu^{2+} in ammonia solution is described by the two-electron step reduction:

$$Cu(NH_3)_4{}^{2+}(aq) + 2e^- \rightarrow Cu(NH_3)_2{}^{+}(aq) + 2NH_3(g) \qquad E^0{}_{SHE} = 0.1\ V$$

$$Cu(NH_3)_2{}^{+}(aq) + e^- \rightarrow Cu\ (s)\ + 2NH_3(g) \qquad E^0{}_{SHE} = -0.1\ V$$

The two-step reduction of copper is explained by the stabilization of Cu^+ in an ammonia complex. Ag^+ in the ammonia-based electrolyte is reduced by the one-electron step reduction:

$$Ag(NH_3)_2{}^{+}(aq) + e^- \rightarrow Ag\ (s)\ + 2NH_3(g) \qquad E^0{}_{SHE} = 0.37\ V$$

The concentration of metals in the electrolyte and the potential of electrodeposition can influence the morphology and composition of the deposited material. For instance, an electrolyte consisting of 0.1 M $Cu(NO_3)_2$ and 7 mM $AgNO_3$, 1 M sodium nitrate, and 0.5 M ammonium hydroxide solution resulted in the deposition of a homogeneous Cu-Ag coating with Ag content of 13 atomic weight percentage. Co-deposition at -0.9 V resulted in the lowest surface roughness of the Cu-Ag coating.[32]

2.4 Galvanic replacement

The galvanic replacement is a spontaneous redox reaction, in which a more noble metal in solution displaces a less noble metal resulting in the formation of a new metal composite. The reaction is driven by the difference in reduction potentials of the two metals, where the reduction potential of the more noble metal is higher than the metal that is oxidized. The larger this potential difference, the more favorable the galvanic replacement. Regarding our system, the reaction

between metallic Cu and Ag^+ will be used to elaborate further on the technique. The reaction is illustrated in Figure 4 and described by the following equation:

$$Cu\,(s) + 2Ag^+(aq) \rightarrow Cu^{2+}(aq) + 2Ag\,(s) \qquad (5)$$

Where the difference in standard reduction potential of the half-reactions is calculated by:

$$E^0{}_{cell} = 0.80 - 0.34 = +0.46\,V\ vs\ SHE$$

The positive difference in reduction potential translates to a negative change in Gibbs free energy, which characterizes a spontaneous reaction. When performing galvanic replacement, the most stable species in an aqueous solution as a function of potential must be considered in the Pourbaix diagram of a metal. For instance, Cu_2O is stable when Cu^{2+} is in a neutral aqueous solution. In this case, galvanic replacement is described by the following reaction:[33]

$$2Cu\,(s) + 2Ag^+(aq) + H_2O \rightarrow Cu_2O\,(s) + 2Ag\,(s) + 2H^+ \qquad (6)$$

Furthermore, additives can be added to the solution to influence the properties of the produced metal composite. For instance, the addition of mild reducing agents leads to better geometric control of the galvanic replacement.[34] Contrary, when an excessively strong reducing agent is added, the galvanic replacement is effectively inhibited leading to the deposition of a metal layer without affecting the substrate. Structure-directing agents can be used to inhibit galvanic replacement with specific crystal planes. For instance, the adsorption of polyvinylpyrrolidone (PVP) adsorbs on the Cu(100) crystal plane protecting it from galvanic replacement. Additionally, adsorption on the Ag(100) crystal plane inhibits the perpendicular growth of Ag, which increases the homogeneity of the galvanic replacement.[35] Lastly, complexing agents can be added, which could alter the metal oxidation state and stoichiometry of the reaction. For instance, when Cl^- is present in the solution, one Ag^+ ion would be able to displace one Cu atom through the formation of a stable Cu(I)Cl complex. Stronger complexing agents are used to decrease the reduction potential, hence making the galvanic replacement more favorable.[33]

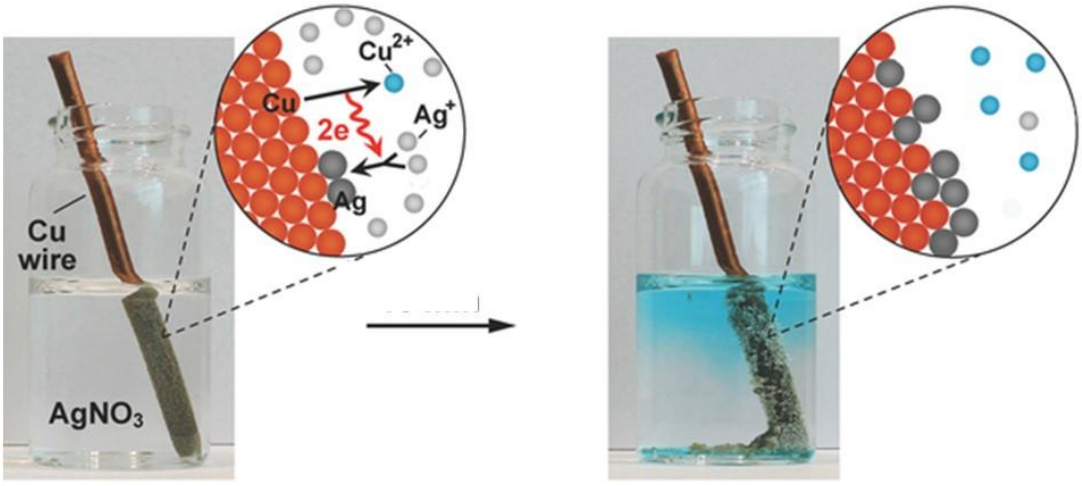

Figure 4. Galvanic replacement by immersion of a Cu wire into an aqueous $AgNO_3$ solution.

Chapter III

Experimental

3.1. Electrode preparation

Commercialized TG-H-060 conductive fuel cell carbon paper was used as the substrate for the catalysts. Circles of 4.9 cm^2 of were pressed out mechanically from a carbon paper sheet. Carbon paper is composed of carbon fibers held together with a binder material forming a 3-dimensional porous structure. Carbon paper has high electrical conductivity and high chemical resistance, making it a suitable substrate for electrocatalytic reactions.[36] But most importantly, the catalytic activity and selectivity of deposited catalysts can be compared without carbon paper contributing significantly to CO_2RR.

3.1.1. Electrodeposited electrodes

An ammonia-based electrolyte was prepared by dissolving 0.1 M copper nitrate trihydrate ($Cu(NO_3)_2 \cdot 3H_2O$), 1 M sodium nitrate ($NaNO_3$), and 0.5 M ammonium hydroxide 28-30% in 100 ml milli-Q water in a glass beaker. The color of the solution turned deep blue due to the formation of the $Cu(NH_3)_4^{2+}$ complex. A customized electrodeposition holder was used to position the carbon paper in the electrolyte, which exposed 3.8 cm^2 of the substrate. The anode platinum wire was positioned in the electrolyte at ~1 cm distance from the substrate. The distance between the substrate and platinum wire was kept as constant as possible but was challenging because they were positioned manually. Then, $5.2 \cdot 10^{-5}$ mol of Cu was deposited using 10 C at -0.7 V vs Ag/AgCl. The potentiostat allowed for determining the cutoff charge, which is the charge made available for electrodeposition. The electrode was rinsed with milli-Q water to remove surface contaminants and dried overnight. This electrode is labeled Cu-ref and is characterized by a red-brown color. For the silver reference, the ammonia-based electrolyte was prepared by dissolving 0.05 M silver nitrate ($Ag(NO_3)$), 1 M $NaNO_3$, 0.5 M NH_4OH, and 0.01 M ethylenediaminetetraacetic acid (EDTA) in 100 ml milli-Q water in a glass beaker. Then, $5.2 \cdot 10^{-5}$ mol of Ag was deposited using 5 C at -0.1 V vs Ag/AgCl. Lastly, the electrode was rinsed and dried overnight. The electrode is labeled Ag-ref and is characterized by a silver color.

To prepare the electrode where Cu and Ag are separated by a gap region, the substrate was covered in the middle by 3 mm non-conducting tape. Both electrolytes described above were prepared. First, on half of the substrate $2.6 \cdot 10^{-5}$ mol Ag was deposited using 2.5 C at -0.1 V vs Ag/AgCl. The substrate was rinsed and dried overnight. A visual check was conducted to ensure no Ag was deposited underneath the tape. Then, electrodeposition was performed on the other half of the substrate $2.6 \cdot 10^{-5}$ mol Cu was deposited using 5 C at -0.7 V vs Ag/AgCl. After the electrode was rinsed and dried overnight, the tape was carefully removed, and the electrode is labeled as Cu-Ag-gap. The same procedure was applied without tape to prepare the electrode where Cu and Ag are interfaced. First, $2.6 \cdot 10^{-5}$ mol Ag was deposited using 2.5 C at -0.1 V vs Ag/AgCl on one half of the substrate. Subsequently, the other half including the boundary of the deposited Ag was

immersed into the Cu electrolyte to create an interface. The electrode was rinsed and dried overnight and labeled as Cu-Ag-int.

For co-deposition, the ammonia-based electrolyte was prepared by dissolving 0.1 M $Cu(NO_3)_2 \cdot 3H_2O$, 7 mM $Ag(NO_3)$, 1 M $NaNO_3$, 0.6 M NH_4OH, and 0.01 M ethylenediaminetetraacetic acid (EDTA) in 100 ml milli-Q water in a glass beaker.[32] The concentration of ammonia solution was increased to prevent precipitation of the light-blue copper(II)hydroxide complex. The co-deposition was performed using 7.5 C at -0.9 V. The electrode is labeled as Cu-Ag-cod and is characterized by a dark blue color.

3.1.2. Galvanically replaced electrodes

Cu-ref was used as the substrate for galvanic replacement. To remove surface copper oxides, the electrode was reduced by linear sweep voltammetry from -0.6 to -1.5 V vs Ag/AgCl in a glass beaker containing 90 mL 0.1 M $NaNO_3$ solution. After reduction, 10 mL of 10 mM $AgNO_3$ solution was added into the beaker under magnetic stirring at 300 rpm. The stirring rate could be adjusted to ensure that no vortex was generated. Samples were prepared after 1, 2, and 3 minutes of galvanic replacement. The electrodes are characterized by black color.

3.1.3. Colloidal synthesis of Cu_2O nanospheres

A synthesis route for Cu nanowires reported by Huaman et al.[20] was used to prepare copper(I)oxide (Cu_2O) nanospheres. Inside a 100 mL reactor, 0.55 mM polyvinylpyrrolidone (PVP) was dissolved in 30 mL ethylene glycol. Then, 10 mM $Cu(NO_3)_2 \cdot 3H_2O$ and 1.25 mM hexadecyltrimethylammonium chloride (CTAC) was dissolved in 15 mL EG in a glass vial. The solution in the glass vial was added to the reactor. While sealed, the reactor was purged with nitrogen above the solution. The pressure inside the reactor was regulated by a Schlenk line. Subsequently, the solution was heated at 180 ˚C for 2.5 h under continuous magnetic stirring at 350 rpm and nitrogen purging. The reaction was terminated by quenching in a cold-water bath and 15 mL product solution was centrifuged thrice in methanol at 3000 rpm for 10 minutes. The precipitate was re-suspended in 15 mL methanol and 2 mL was drop-casted onto carbon paper. The electrode is labeled as Cu_2O-ref. The galvanic replacement was performed on Cu_2O-ref with 1 mM $AgNO_3$ solution following the same procedure as described above. Samples were prepared after 0.5, 1, 2, and 4 minutes of galvanic replacement. The electrodes are labeled as Cu_2O-Ag-*t*, where t = 0.5, 1, 2, or 4.

3.2. Catalytic testing

The catalytic performance of the CO_2RR was tested in the customized H-cell illustrated in Figure 5. The glassy carbon disk was placed behind the electrode to provide mechanical strength and prevent the electrolyte to leak from the cathodic half-cell. The 3 M Ag/AgCl reference electrode is positioned in the cathodic half-cell close to the cathode. The platinum disk is placed in the anodic half-cell and functions as the counter electrode. The half-cells are filled with 15 mL 0.1 M potassium bicarbonate solution and are separated by an N-117 proton exchange membrane. CO_2 (g) is bubbled into the cathodic half-cell with 10 mL/min, while Ar (g) is bubbled into the anodic half-cell. The electrolyte in the cathodic half-cell is saturated for 30 minutes with CO_2 under magnetic stirring, which causes the pH of the electrolyte to drop to 6.8.

Figure 5. Disassembled H-cell used for catalytic testing of the CO_2RR. On the left-hand side, the cathodic half-cell is shown separated from the anodic half-cell by the proton exchange membrane, which is displayed in the center. The carbon paper is depicted as the smaller darker circle on top of the larger glassy carbon disk. The Ag/AgCl electrode is connected to the potentiostat by the blue wire. The platinum disk is shown in the anodic half-cell, which like the glassy carbon disk, is connected to the potentiostat through the copper connections.

After the electrolyte is saturated with CO_2, linear sweep voltammetry was performed to reduce the catalyst. This was done in the potential range of -0.6 to -1.5 V vs Ag/AgCl. For catalytic testing, chronoamperometry was applied for 30 minutes at -0.9, -1.1, -1.3, -1.5, -1.7, -1.8, and -2.0 V vs Ag/AgCl. During CO_2RR, analysis of gaseous products was performed by CompactGC$^{4.0}$. Every three minutes a sample was injected into the gas chromatography column, from which in total ten data points per potential were obtained. Analysis of liquid products was performed with NMR by the Varian MRF 400 MHz spectrometer. A sample was prepared by adding 100 µL internal standard (10 mM dimethyl sulfoxide and 50 mM phenol solution) to 500 µL catholyte.

From the product analysis and total current measured by the potentiostat, the current utilized for a specific product can be calculated. Normalizing this to the geometric area of the electrode gives

us the partial current density. In electrochemistry, this property is used as a measure of catalytic activity, which is calculated through the following formula:

$$Partial\ current\ density\ = \frac{z \times F \times n}{A}$$

Where z is the number of electrons transferred, F is the Faraday constant = 96485 C/mol, n is the moles of product formed and A is the geometric surface area of the catalyst. The fraction of the total current that is utilized for a specific product is defined as the Faradaic efficiency (FE) and is used as a measure of catalytic selectivity in electrochemistry:

$$Faradaic\ Efficiency = (\frac{z \times F \times n}{I \times t}) \times 100$$

Where *z* is the number of electrons transferred, F is the Faraday constant = 96485 C/mol, *n* is the moles of product formed, *I* is the total current in amperes and *t* is the total reaction time. In practice, the Faradaic efficiency of products does not sum up to 100% because the system is not perfectly sealed, leading to leakage of electrolytes, current, and gasses. Therefore, there is a missing Faradaic efficiency that accounts for the current that has not been used for CO_2 reduction or HER.

3.3. Characterization of electrodes

Identification of crystal phases present in the catalysts was analyzed by a Bruker D2 Phaser X-ray diffractometer using Co-Kα_1 radiation. Typical spectra are measured one second per data point in the 2θ range of 20-80˚, with an increment of 0.02-0.03˚ and a rotational increment of 15˚/min. Morphology was studied using scanning electron microscopy (SEM) on the Phenom Pro Desktop. A typical SEM image was obtained at 10 kV with a back-scatted full detector via Phenomworld software. The elemental composition of a catalyst was analyzed by energy-dispersive X-ray at 15 kV on the Phenom Pro Desktop. Morphology was also studied with high-resolution using the Helios 5 DualBeam in Field-Free SEM mode at 10 kV with an Everhart-Thornley detector. High-resolution analysis of the elemental composition was performed by energy-dispersive X-ray spectroscopy (EDX) at 15 kV. Transmission electron microscopy (TEM) was used to obtain information about the morphology and diameter in higher resolution than could be obtained in SEM mode.

3.4. Materials

$Cu(NO_3)_2 \cdot 3H_2O$ (CAS: 10031-43-3), $AgNO_3$ (CAS: 7761-88-8), CTAC (CAS: 112-02-7), and PVP with average mol weight 40 (CAS: 9003-39-8) were obtained from Sigma-Aldrich. Ammonia solution 28-30% (CAS: 1336-21-6) was obtained from Supelco®. $NaNO_3$ (CAS: 7631-99-4) and ethylene glycol (CAS: 107-21-1) were obtained from Thermo Scientific Chemicals.

Chapter IV

Results and discussion

This chapter is divided into two parts, where in the first part the Cu-Ag catalysts that were prepared via electrodeposition, co-deposition, and galvanic replacement are characterized and evaluated in the CO_2RR. In the second part, the Cu_2O-Ag catalysts prepared by colloidal synthesis and galvanic replacement are characterized and evaluated in the CO_2RR. The prepared electrodes are summarized in Table 2.

Table 2. Sample ID of the catalysts that are characterized and tested for the CO_2RR.

Metallic composition	Preparation	Sample ID
Cu	electrodeposition	Cu-ref
Ag	electrodeposition	Ag-ref
Cu-Ag	electrodeposition	Cu-Ag-gap
Cu-Ag	electrodeposition	Cu-Ag-int
Cu-Ag	co-deposition	Cu-Ag-cod
Cu-Ag	electrodeposition + galvanic replacement	Cu-Ag-gr
Cu_2O	colloidal synthesis	Cu_2O-ref
Cu_2O-Ag	colloidal synthesis + galvanic replacement	Cu_2O-Ag-*t*

4.1. Characterization of Cu-Ag electrodes

To study the crystal structure of the reference and Cu-Ag electrodes, the XRD spectra are shown in the 2θ range from 40˚ to 80˚ in Figure 6. The XRD spectra are normalized to the peak with the highest intensity at 30.8˚, which is attributed to graphite from the carbon paper. Another peak of graphite is observed at 64.1˚. The crystal planes that can be identified in Cu-ref are Cu(111) at 50.8˚ and Cu(200) at 59.3˚. For Ag-ref, the crystal planes Ag(111) at 44.6˚, Ag(200) at 51.9˚, and Ag(220) at 76.6˚ can be identified. The crystal planes Cu(111), Cu(200), Ag(111), Ag(200) and Ag(220) are identified in Cu-Ag-gap and Cu-Ag-int at identical 2θ angles. In the spectrum of Cu-Ag-cod, two broad peaks with low intensity are detected at 44.7˚and 49.8˚. To study these peaks, the magnification of the denormalized spectrum in the 2θ range from 40˚ to 55˚ is shown in Figure 7. From this spectrum, the two peaks can be identified as Ag(111) at 44.6˚ and a shifted Cu(111) peak at 50.1˚. For an arbitrary Cu-Ag-gr electrode, the Cu(111) and Cu(200) crystal planes can be identified. In Figure 7, the denormalized spectrum magnified in the 2θ range from

40˚ to 55˚ is shown, in which a very weak peak is detected at 44.6˚, which could correspond to the Ag(111) crystal plane.

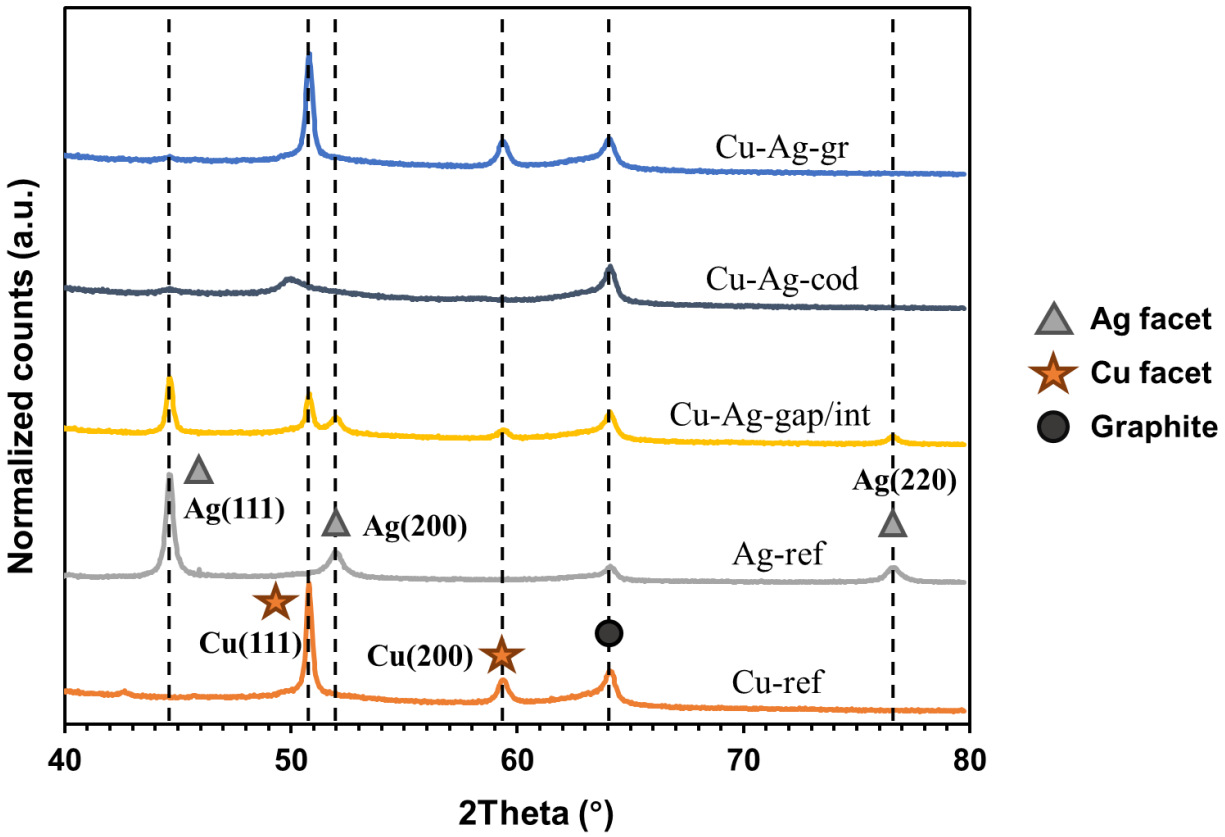

Figure 6. X-ray diffraction spectra in the 2θ range from 40˚ to 80˚ of the Cu-Ag electrodes.

The normalized XRD spectra in Figure 6 show that the electrodes prepared by electrodeposition resulted in the deposition of non-preferentially oriented crystals containing multiple crystal planes. The (220) crystal plane of Cu-ref is not detected, because this peak is expected to be detected at larger 2θ angles than was measured.[37] The relative intensity of a peak indicates the prevalence of a crystal plane in the deposited material. For Cu-Ag-gap and Cu-Ag-int, the same peaks are identified as in Cu-ref and Ag-ref. The relative intensities of the peaks correspond to the reference catalysts and the absolute intensities are approximately half compared to the reference electrodes because half of the moles of each metal were deposited. From this, it can be concluded that segregated phases of Cu and Ag were deposited. For Cu-Ag-cod, the Ag(111) and Cu(111) crystal planes can be identified in Figure 7, but the Cu(111) facet is shifted to a smaller 2θ angle by 0.7˚. This could indicate that the lattice spacing between Cu atoms in Cu(111) increased according to Bragg's law. This can be explained by the incorporation of a larger Ag atom. The peak shift should be proportional to the metal ratio of the deposited material. Considering the molar ratio of Cu to Ag in the electrolyte (14.3:1), the peak is expected to be detected close to the Cu(111) peak. However, considering the broad and low-intensity signals of both peaks, it is suggested that presumably an amorphous phase was deposited without crystalline

phases. This explanation is more plausible because broad and low-intensity peaks have been observed in previous studies for thick amorphous coatings.[38] The crystal planes of Cu-Ag-gr that can be identified in Figure 6 correspond to Cu(111) and Cu(200). These peaks are expected because galvanic replacement primarily affects the surface of the Cu-ref substrate. Additionally, a broad and low-intensity peak corresponding to Ag(111) can be identified in Figure 7. Differently from Cu-Ag-cod, the characteristics of this peak can be explained by that galvanic replacement has occurred primarily on the surface of Cu-ref, which can be detected by a very weak signal lost in background noise.

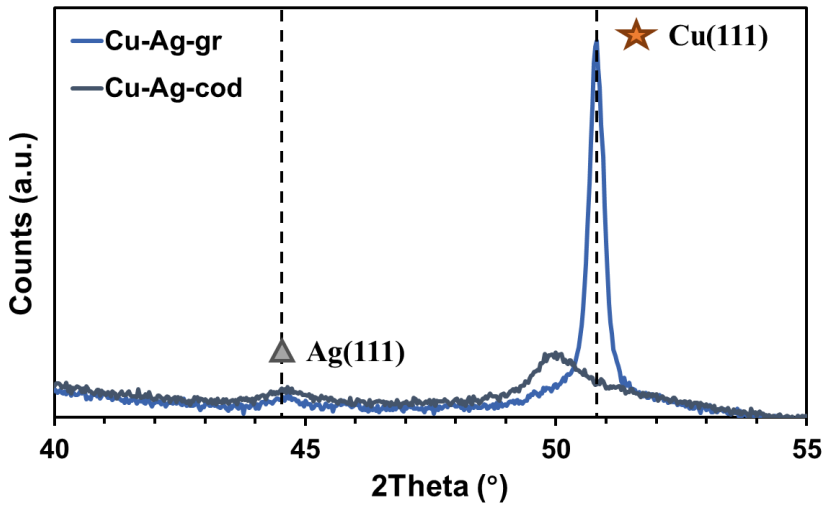

Figure 7. Denormalized XRD spectrum in the 2θ range from 40˚ to 55˚.

Scanning electron microscopy was performed to study the relation between the crystal structure and the external shape of the deposited materials. With this technique, micrographs are produced by scanning the surface of a sample with a focused beam of electrons. To have comparable catalyst loading in the electrode, the coverage of the carbon paper is considered. The initial two micrographs of Cu-ref and Ag-ref in Figure 8 show that the front carbon fibers are covered by a continuous coating. Upon further magnification, it is observed that the non-preferential oriented metals possess spherical particle morphology rather than being a film. The average particle size of Cu-ref is 1.6 µm with a standard deviation of 0.48 µm. For Ag-ref, the average particle size is 1.9 µm with a standard deviation of 0.39 µm. The average particle size was measured as an average over the diameter of 220 arbitrary particles (Figure A1 – Particle size distribution).

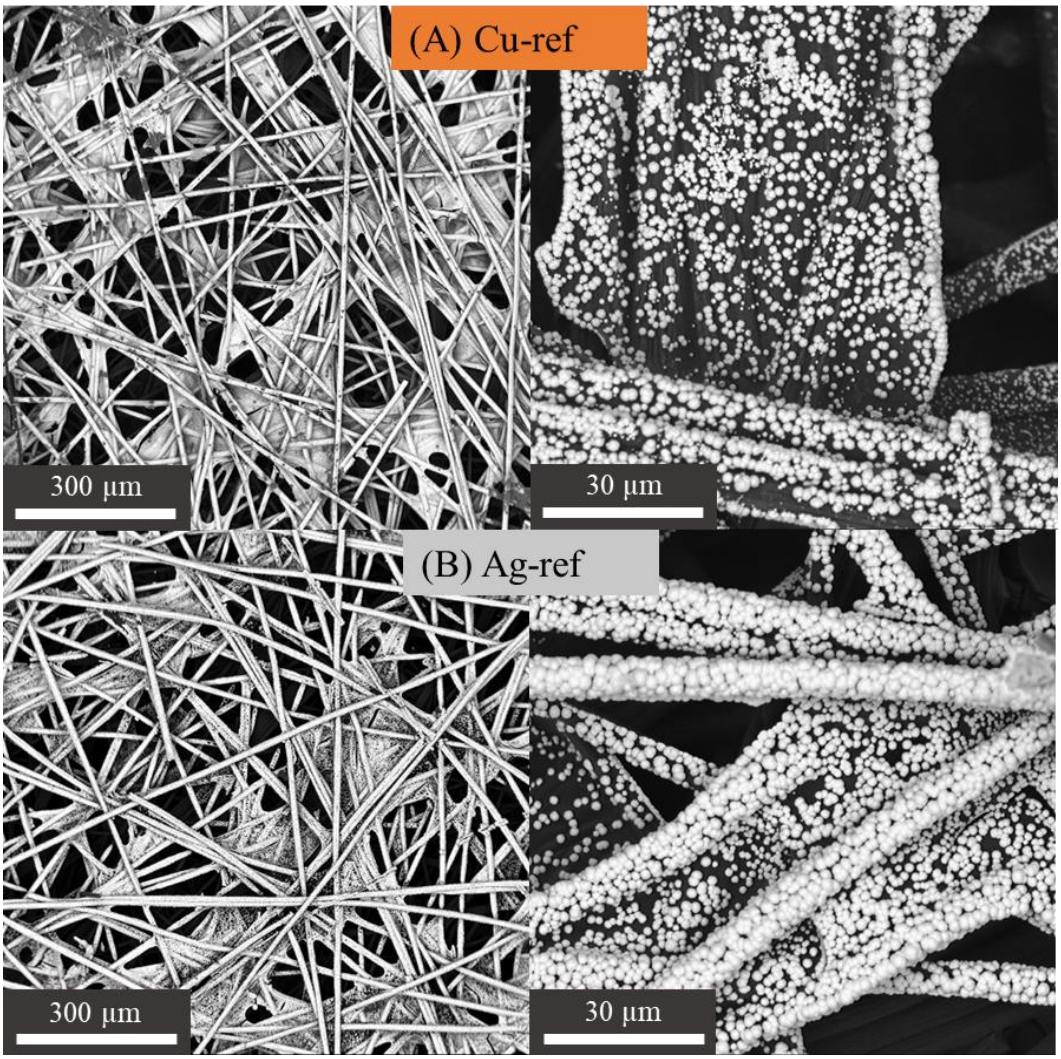

Figure 8. Micrographs obtained with SEM: (A) Cu-ref (B) and Ag-ref appear as continuous coating deposited on the front carbon fibers of the carbon paper. Upon further magnification, the deposited materials appear as particles with spherical morphology.

The Cu-Ag-gap and Cu-Ag-int electrodes are investigated with scanning electron microscopy to determine the distance between the two metals. An identical coverage of the carbon paper and particle morphology was observed as in the reference electrodes (Figure A2). As given in Figure 9A, the metals in Cu-Ag-gap are separated by 2.9 mm, exposing carbon paper in this region. The interface of the metals in Cu-Ag-int is identified by the difference in particle size, as is shown in Figure 9B. It must be noted that the morphology of the Ag particles appears less uniform than was observed for Ag-ref in Figure 8D. This can be explained by the deposition of Cu on top of the boundary of the Ag half to create interfacial contact.

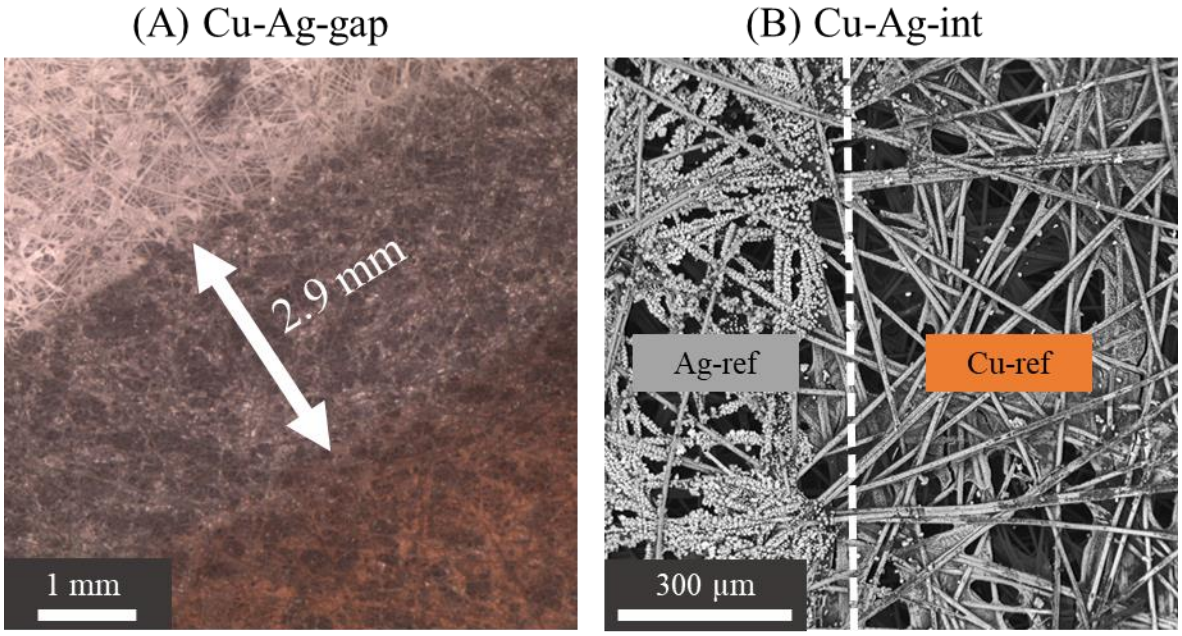

Figure 9. Micrographs obtained with SEM: (A) The gap region of Cu-Ag-gap is 2.9 mm and (B) the interface of Cu-Ag-int identified by the difference in particle size.

Scanning electron microscopy and energy dispersive X-ray analysis with high resolution were performed to study the morphology and distribution of the metals in Cu-Ag-cod. As given in Figure 10A, co-deposition resulted in a continuous coating covering the front carbon fibers, which was also observed in the reference electrodes. Upon magnification by the micrograph of Figure 10B, it becomes apparent that the deposit also exhibits spherical particle morphology. In Figure 10C and 10D, the two micrographs represent the energy X-ray dispersive analysis of Cu and Ag, respectively, where the intensity of the colors (Cu = red and Ag = cyan) are proportionate to the presence of the metal. The analysis shows that Cu and Ag are homogeneously distributed over the particle surface with an atomic ratio of 3.5:1, respectively. Furthermore, weak detection of oxygen was observed at the surface of the particles, which is likely due to surface oxidation in atmospheric conditions (Figure A3).

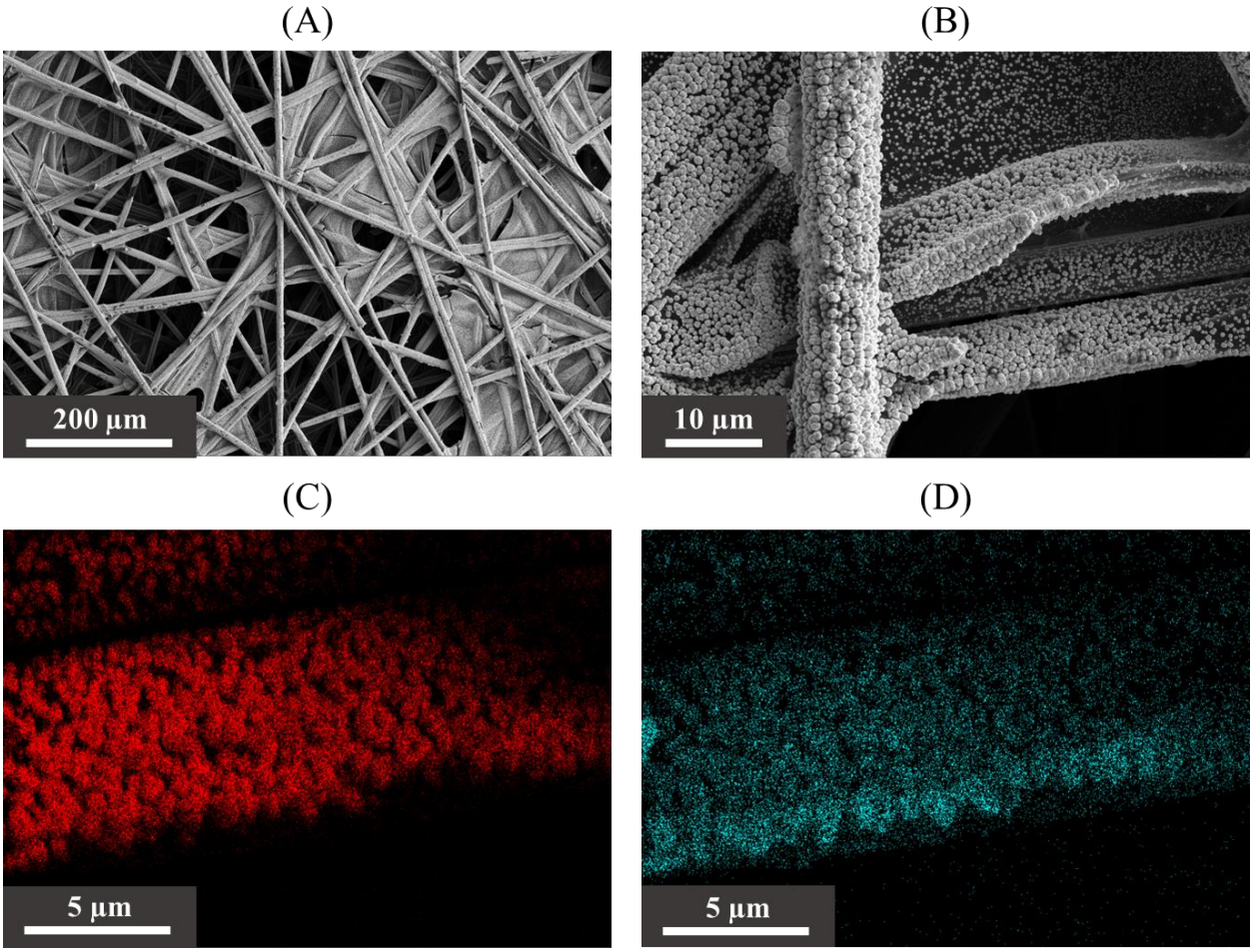

Figure 10. Micrographs of Cu-Ag-cod obtained with high-resolution SEM: (A) The deposited material appears as a continuous film covering the front fibers of the carbon paper. (B) Upon magnification, particles appear with spherical morphology. Energy dispersive X-ray analysis shows the (C) detection of Cu indicated in red and (D) Ag in cyan.

Three electrodes were prepared after 1, 2, and 3 minutes of galvanic replacement by immersion of Cu-ref into a 1 mM $AgNO_3$ solution. Scanning electron microscopy was performed to study the evolution of morphology with increasing reaction time. The micrographs are given in Figure 11, which display that the morphology of Cu-ref is preserved, and dendritic Ag is deposited on top due to galvanic replacement. This shows that galvanic replacement primarily occurred at the surface of the particles, explaining the broad and low-intensity peak corresponding to Ag(111) observed with XRD. A longer duration of galvanic replacement resulted in increased growth of Ag dendrites. It is aimed to prevent the growth of large Ag dendrites because it would significantly change the morphology of Cu-ref, rendering it unsuitable for comparison with the other electrodes. Nonetheless, it is essential to introduce a significant amount of Ag to generate enough CO-producing sites increasing the abundance of *CO. After 1 minute of galvanic replacement, the formation of very few and small Ag dendrites can be observed. When the reaction time is increased to 2 minutes, an even distribution of larger Ag dendrites on the front carbon fibers can be observed. Finally, if the reaction time is further increased to 3 minutes, large clusters of Ag dendrites can be

found rather than evenly distributed dendrites. Additionally, the surface ratios of Cu to Ag were measured by energy-dispersive X-ray analysis. The surface ratios were measured at 31.8:1, 5.1:1, and 1.3:1 after 1, 2, and 3 minutes, respectively. Since the Ag dendrites are medium-sized and evenly distributed, the morphology of Cu-ref can still be observed, and a surface ratio of 5.1 was measured, the electrode prepared after 2 minutes of galvanic replacement is studied further. This electrode will be referred to as Cu-Ag-gr from now on.

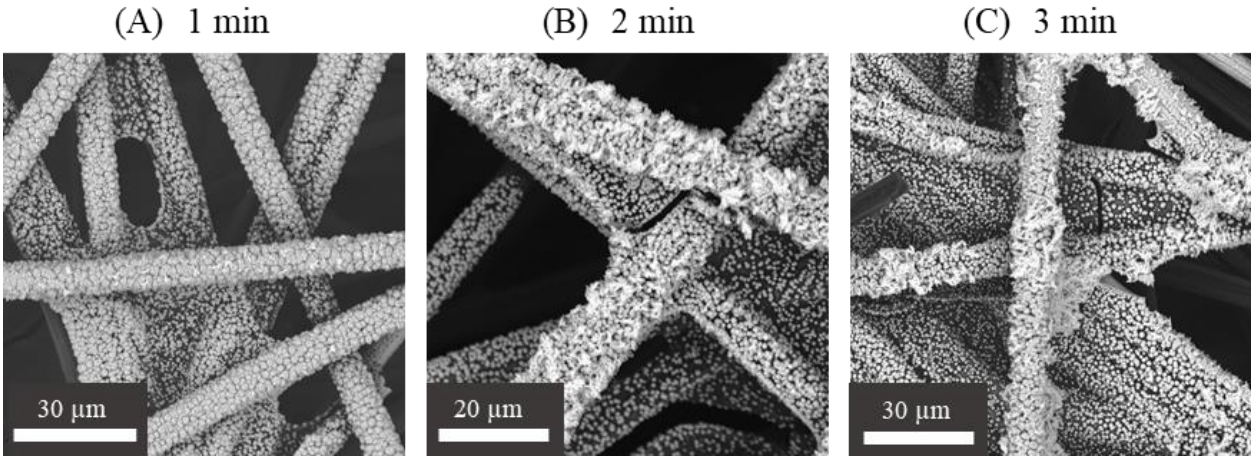

Figure 11. Micrographs obtained with SEM: The evolution of the morphology of Cu-ref by the galvanic replacement using a 1 mM $AgNO_3$ solution after (A) 1 minute, (B) 2 minutes, and (C) 3 minutes.

To study the distribution of Cu and Ag further, high-resolution scanning electron microscopy and energy-dispersive X-ray analysis were performed. The high-resolution micrographs of Cu-Ag-gr are provided in Figure 12. The first image shows that the coverage of the front carbon fibers remains identical to Cu-ref after galvanic replacement. Upon magnification in Figure 12B, it can be observed that the morphology of the Cu particles on the back fibers is intact, while the particles on the front fibers appear to be partially covered, presumably by galvanically replaced Ag. However, the dendritic growth of Ag has not been observed as it was seen with SEM in Figure 11B. This lack of observation may be due to the absence of contrast in the detection of Cu and Ag in the micrograph shown in Figure 12B. Based on this observation, it cannot be determined whether the Ag dendrites grow perpendicular or parallel to the surface of the Cu particles. To investigate this further, an energy-dispersive X-ray analysis was performed, from which the color maps of Cu and Ag are shown in Figures 12C and 12D, respectively. It is confirmed that the Cu particles on the back carbon fibers remain intact after galvanic replacement. Based on both images, it can be concluded that a layer of Ag has formed around the Cu-ref on the front carbon fibers, resulting in a Cu to Ag surface ratio of 1.8:1. Combining this with the Ag dendrites observed in Figure 11B, it may be concluded that Ag dendrites grew parallel to the surface of the Cu particles rather than perpendicular. This observation suits the mechanism of galvanic replacement, where Cu atoms are oxidized by Ag^+ ions. Furthermore, unaffected Cu clusters with alternative morphology are observed on top of the Ag layer. This could be attributed to the redeposition of Cu or Cu_2O on the deposited Ag layer, as both species are stable at neutral pH (Figure A4 – Pourbaix diagram[39]). Presumably, the redeposition of Cu_2O is observed, because

the galvanic replacement was performed in an aerated environment. However, evidence for this mechanism is not provided in this study. Finally, the detection of oxygen was observed (Figure A5) due to surface oxidation in atmospheric conditions.

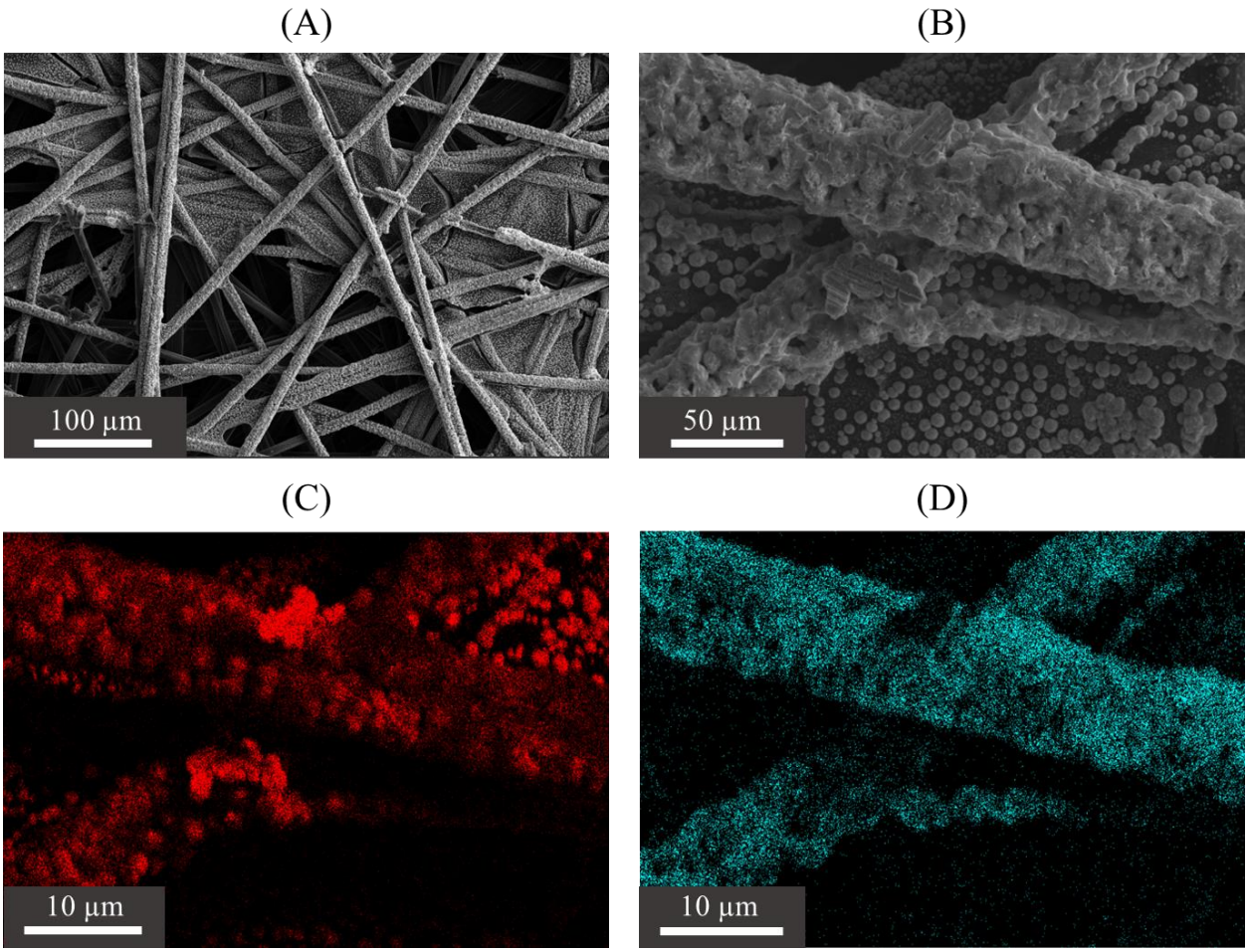

Figure 12. Micrographs of Cu-Ag-gr showing (A) the coverage of carbon paper and (B) surface-modified particles on the front carbon fibers. Energy dispersive X-ray analysis of (C) Cu in red and (D) Ag in cyan.

In this section, four electrodes have been characterized with X-ray diffraction, scanning electron microscopy, and energy-dispersive X-ray analysis to study the crystal structure, morphology, and distribution of Cu and Ag. Additionally, Cu-ref and Ag-ref were prepared as a reference. From the crystal structure of the references the (100), (200), and (220) crystal planes could be identified. The morphology of the reference electrodes exhibits spherical particle shape and are a few µm in diameter. For Cu-Ag-gap and Cu-Ag-int, it was confirmed with XRD that Cu and Ag are deposited as segregated phases because all the crystal planes could be identified that were detected in the reference electrodes. From the micrographs of Cu-Ag-gap, it was measured that a 2.9 mm gap was created. For Cu-Ag-int, an interface region was observed by the difference in particle size of Cu and Ag. For Cu-Ag-cod, it is suggested an amorphous phase is deposited because two broad and low-intensity peaks were observed corresponding to Cu(111) and Ag(111). Morphology-wise, spherical particles were still observed with HR-SEM, and with EDX it was

shown that Cu and Ag are homogenously distributed at the surface of these particles with a Cu to Ag ratio of 3.5:1. Finally, for Cu-Ag-gr, a broad and low-intensity peak corresponding to Ag(111) was identified, additional to the crystal planes of Cu-ref. This peak can be explained by that galvanic replacement has mostly occurred at the surface without affecting the bulk Cu. The electrode prepared after 2 minutes is used to study further because evenly distributed and medium-sized Ag dendrites were observed with SEM. Finally, with high-resolution SEM a layer of Ag was observed on top of Cu-ref, resulting in a Cu to Ag surface ratio of 1.8:1. Now that the distribution of Cu and Ag in the electrodes have been characterized, their catalytic activity and selectivity can be evaluated in the CO_2RR.

4.2. Catalytic properties of Cu-Ag electrodes

The current density (j) is used to evaluate the catalytic activity of CO_2RR, while the Faradaic efficiency (FE) is used to evaluate the catalytic selectivity. The gaseous products will be analyzed to study the production of hydrogen, CO, methane, and ethylene. These are important products for studying ethylene production because CO is considered a key intermediate, while hydrogen and methane compete in the production of ethylene. Therefore, analyzing these products can provide insights into the efficiency of the CO_2RR towards ethylene. Ethane is typically produced in trace amounts and can therefore be excluded from the discussion. Additionally, the production of liquid products in the electrolyte will be analyzed after the CO_2RR to evaluate the total Faradic efficiency towards liquid products.

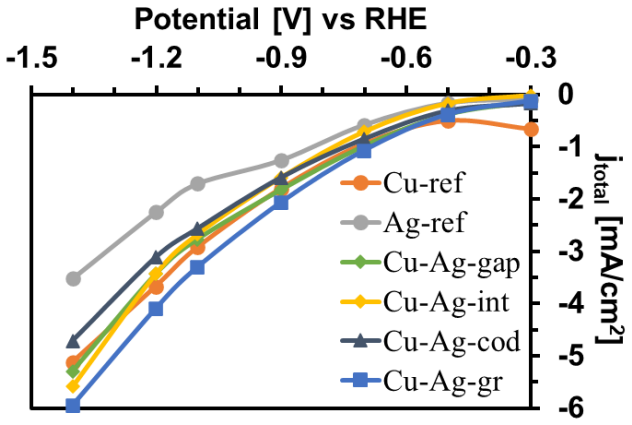

Figure 13. Total current density of the CO_2RR using Cu-Ag electrodes.

The total current density (j_{total}) of the CO_2RR using the as-prepared electrodes is given in Figure 13. In general, the current density increases as the reduction potential increases, following Ohm's law.[40] The non-zero total current density measured at -0.3 V vs RHE can be attributed to the reduction of surface oxides and the HER. The total current density of Ag-ref is lower at all potentials compared to Cu-ref. This could be explained by the reduced catalytic surface area due to larger particles. Another possibility could be that the CO_2RR was measured with different cell resistance, causing the current density of Ag-ref to belong to lower potentials. However, this has not been considered and should be done in follow-up research. The total current density of Cu-Ag-gap and Cu-Ag-int exceeds that of Cu -ref at -1.4 V vs RHE, which could be attributed to enhanced CO_2RR at higher potentials due to increased *CO abundance. Consequently, the total current density of Cu-Ag-int is higher than that of Cu-Ag-gap at -1.4 V vs RHE due to higher *CO abundance through an interface. The total current density of Cu-Ag-cod is lower than the other Cu-Ag electrodes. This can be attributed to less deposited metals via co-deposition using 7.5 C. Because it is not determined how the charge is divided for Cu and Ag deposition, the final deposited moles of metals may be reduced resulting in lower current density. Finally, Cu-Ag-gr

exhibits overall the highest current density, which indicates that the total activity increases compared to Cu-ref due to galvanic replacement. To determine what contributes to the differences in the total current densities, the partial current densities for hydrogen, CO, methane, and ethylene are given in Figure 14. From this point forward, the potentials will be described vs RHE.

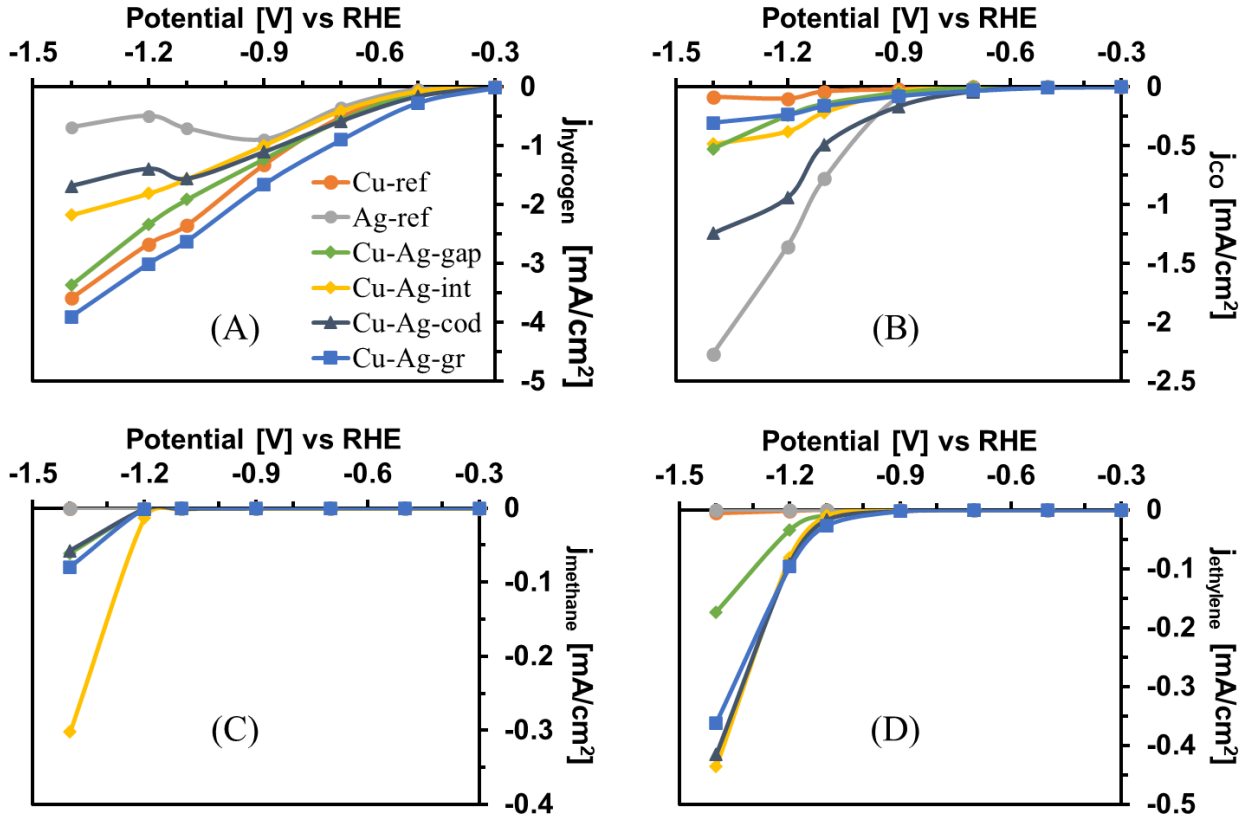

Figure 14. Partial current densities for (A) hydrogen, (B) CO, (C) methane, and (D) ethylene of the Cu-Ag electrodes.

At -1.4 V, the partial current densities for Cu-ref are $j_{hydrogen}$ = -3.6 mA/cm^2, j_{CO} = -0.084 mA/cm^{-2}, and $j_{ethylene}$ = -0.0052 mA/cm^2. The low values for j_{CO} and $j_{ethylene}$ are due to the poor CO_2RR activity of Cu, favoring the HER. The j_{CO} value peaks at -1.2 V, indicating that more *CO is made available for further reduction to ethylene at -1.4 V. The partial current densities for Ag-ref are $j_{hydrogen}$ = -0.69 mA/cm^2 and j_{CO} = -2.3 mA/cm^{-2} at -1.4 V. The j_{CO} value increases with increasing potential, while $j_{hydrogen}$ decreases at -1.2 V. This suggests that Ag is a good catalyst for CO production in CO_2RR. For Cu-Ag-cod, the partial current density values are $j_{hydrogen}$ = -1.7 mA/cm^2, j_{CO} = -1.2 mA/cm^{-2}, $j_{methane}$ = -0.057 mA/cm^2, and $j_{ethylene}$ = -0.42 mA/cm^2 at -1.4 V. A similar decrease in the $j_{hydrogen}$ value is observed as for Ag-ref, exhibiting the HER suppressing character of Ag. The j_{CO} value approaches a plateau at -1.4 V, indicating that CO is reduced further at higher potentials, which leads to an increase in $j_{methane}$ and $j_{ethylene}$. For Cu-Ag-gap, the partial current density values are $j_{hydrogen}$ = 3.4 mA/cm^2, j_{CO} = -0.52 mA/cm^2, $j_{methane}$ = -0.061 mA/cm^2, and $j_{ethylene}$ = -0.17 mA/cm^2 at -1.4 V. The decrease in $j_{hydrogen}$ compared to Cu-ref can be attributed to the addition of Ag, which reduces the activity for hydrogen production. The activity for CO production increases by Ag, which presumably also leads to an increased abundance of *CO on

the Cu surface through synergy, resulting in the promotion of ethylene production and suppression of the HER. If the metals are interfaced, the partial current density values are $j_{hydrogen}$ = 2.18 mA/cm^2, j_{CO} = -0.49 mA/cm^2, $j_{methane}$ = -0.30 mA/cm^2, and $j_{ethylene}$ = -0.44 mA/cm^2 at -1.4 V. The further decrease in $j_{hydrogen}$ indicates that the HER is more suppressed, which can be attributed to enhanced synergy between the metals. This enhanced synergy is established by a 5-fold increase in methane production and a 2.6-fold increase in ethylene production. Furthermore, the value for j_{CO} approaches a plateau at -1.4 V, which can be explained by the limited production of CO due to more effective synergy. For Cu-Ag-gr, the partial current density values are $j_{hydrogen}$ = -3.9 mA/cm^{-2}, j_{CO} = -0.30 mA/cm^{-2}, $j_{methane}$ = -0.080 mA/cm^{-2} and $j_{ethylene}$ = -0.36 mA/cm^{-2} at -1.4 V. The increase in $j_{hydrogen}$ indicates poor CO_2RR activity and the increase in j_{CO} suggests that CO-producing sites that are not involved in synergy have been added. However, the 70-fold increase in $j_{ethylene}$ indicates that the majority of galvanically replaced Ag contributes to the production of ethylene through synergy. Based on the current densities, it can be concluded that synergy is created when Cu and Ag are deposited as segregated systems. Interfacial contact increases the abundance of *CO on the Cu surface and suppresses the HER compared to separated metals. When contact between Cu and Ag is created via galvanic replacement, a significant boost in activity for ethylene production is observed. Subsequently, the Faradaic efficiency needs to be evaluated to assess how efficiently electrons are used for ethylene, CO, and its competing products.

The Faradaic efficiency towards the gaseous products is given at -1.4 V in Figure 15 because the difference in FE is more evident at higher potentials. The current that was not utilized for CO_2RR to gaseous products or HER is indicated as missing. For Cu-ref, $FE_{hydrogen}$ is 70% due to the poor activity for CO_2RR favoring hydrogen production. Consequently, $FE_{CO,}$ $FE_{methane,}$ and $FE_{ethylene}$ are 1.6%, 0.0%, and 0.1%, respectively. The higher selectivity for CO compared to ethylene can be attributed to the low abundance of *CO, which hinders *CO dimerization favoring the release of CO (g). For Ag-ref, FE_{CO} and $FE_{hydrogen}$ are 66% and 17%, respectively, due to the good activity of Ag for CO_2RR. For Cu-Ag-gap, $FE_{hydrogen}$, FE_{CO}, $FE_{methane,}$ and $FE_{ethylene}$ are 63%, 9.9%, 1.1%, and 3.3%, respectively. The relatively low FE_{CO} and increased $FE_{methane}$ and $FE_{ethylene}$ compared to Cu-ref can be explained by the effective transfer of CO from Ag to Cu. For Cu-Ag-int, $FE_{hydrogen}$, FE_{CO}, $FE_{methane,}$ and $FE_{ethylene}$ are 39%, 8.7%, 3.3%, and 7.8%, respectively. Compared to Cu-Ag-gap, a further decrease in FE_{CO} of -1.2% and an increase in $FE_{methane}$ and $FE_{ethylene}$ of +2.2% and +4.5% are observed, respectively. Furthermore, a significant decrease in $FE_{hydrogen}$ of -27% is observed. Based on these observations, it can be concluded that more effective synergy occurs between Ag and Cu due to the interface. Hypothetically, this is caused by an increase in the number of Ag CO-producing sites that are involved in synergy. Consequently, Cu becomes more active, and the $FE_{hydrogen}$ shows a 1.6-fold decrease compared to Cu-Ag-gap.

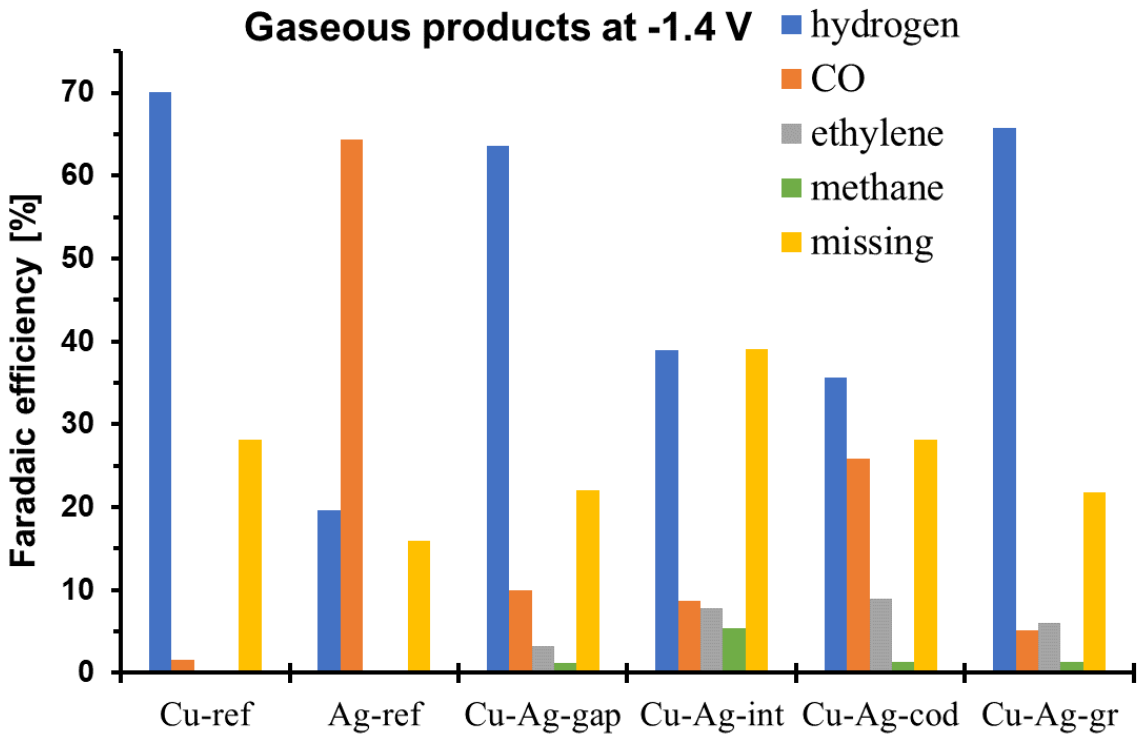

Figure 15. Faradaic efficiency towards the major gaseous products at -1.4 V vs RHE.

For Cu-Ag-cod, $FE_{hydrogen}$, FE_{CO}, $FE_{methane,}$ and $FE_{ethylene}$ are 36%, 26%, 1.3%, and 9.0%, respectively. This is the lowest $FE_{hydrogen}$ observed among the Cu-Ag electrodes, which can be attributed to the incorporated HER-suppressing character of Ag. In addition, the highest FE_{CO} is observed, which indicates that many CO-producing sites are created and synergy between Cu and Ag is not the most effective. This could be related to the homogenous distribution of the metals, by which the *CO abundance is relatively low on neighboring Cu atoms.[30] Nevertheless, the highest $FE_{ethylene}$ is observed, which then indicates that synergy is strongly present, assuming that the amorphous phase detected by XRD contains independent Cu and Ag sites. For Cu-Ag-gr, $FE_{hydrogen}$, FE_{CO}, $FE_{methane,}$ and $FE_{ethylene}$ are 66%, 5.1%, 1.3%, and 6.0%, respectively. The $FE_{hydrogen}$ is approximately the same as for Cu-ref, indicating poor selectivity for the CO_2RR. Compared to Cu-ref, FE_{CO}, $FE_{methane,}$ and $FE_{ethylene}$ show an increase of +3.4%, +1.3%, and +5.9%. This makes Cu-Ag-gr unique in that it is characterized by a $FE_{ethylene}$ greater than its FE_{CO}. This property suggests that the most effective synergy can be generated by the deposition of Ag through galvanic replacement. However, the catalyst still has very high $FE_{hydrogen}$ due to poor activity for CO_2RR, which is probably due to exposure of the Cu-ref substrate to the electrolyte. An approach to overcome this problem could be to adjust the reaction conditions of the galvanic replacement to generate more Ag sites that are involved in synergy to enhance ethylene production while suppressing the HER.

The level of synergy in the CO_2RR can be evaluated using the ethylene/CO ratio, which measures how effectively CO is used as a key intermediate in the reaction pathway towards ethylene. A low value implies that a small amount of ethylene is produced relative to CO, indicating poor synergy of the electrode. Conversely, a high value implies that a high amount of ethylene is produced compared to CO, indicating that CO is being effectively used as a key intermediate in ethylene production. The ethylene/CO ratio of the electrodes in the CO_2RR is given in Figure 16. The onset potential for CO and ethylene production is -0.9 V, and the ethylene/CO ratio increases with a higher potential. This may be caused by increased production of CO, which results in a higher abundance of *CO that promotes *CO dimerization. The ethylene/CO ratio is evaluated at -1.4 V because ethylene production is favored with higher potential. Cu-ref showed the lowest $j_{ethylene}$ and $FE_{ethylene}$ values, resulting in an ethylene/CO ratio of 0.010. Cu-Ag-gap showed an increase in $j_{ethylene}$ and $FE_{ethylene}$ compared to Cu-ref due to synergy resulting in an ethylene/CO ratio of 0.055. Cu-Ag-int showed an increase in $j_{ethylene}$ and $FE_{ethylene}$ compared to Cu-Ag-gap, resulting in a 2.7-fold higher ethylene/CO ratio of 0.15. Although $j_{ethylene}$ and $FE_{ethylene}$ for Cu-Ag-cod are approximately the same as for Cu-Ag-int, the higher values of j_{CO} and FE_{CO} resulted in a lower ethylene/CO ratio of 0.13. However, j_{CO} approaches a plateau, which could indicate that the ethylene/CO ratio might increase at higher potentials. Cu-Ag-gr showed the highest ethylene/CO ratio of 0.18 at -1.4 V, suggesting that galvanic replacement generates Ag sites with the most effective synergy. Therefore, galvanic replacement can be considered a promising method to synthesize a catalyst with enhanced catalytic activity and selectivity for the CO_2RR towards ethylene.

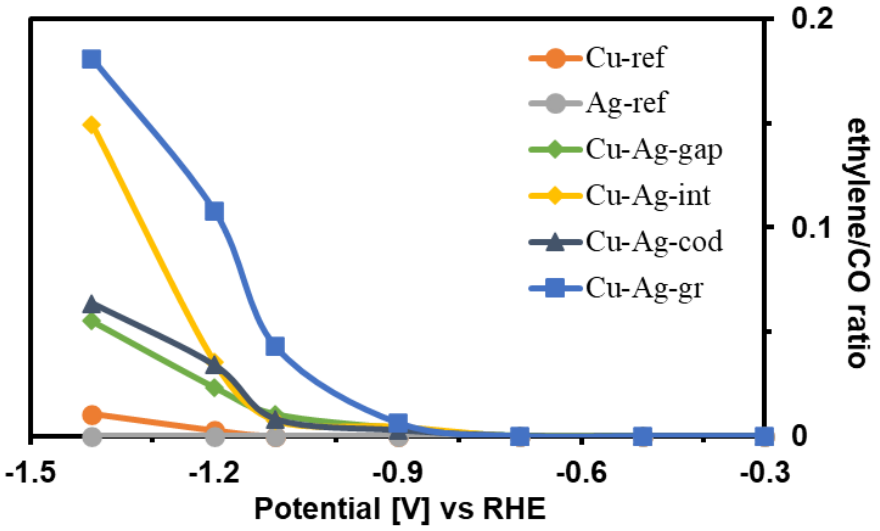

Figure 16. The ratio between ethylene and CO production as a function of potential.

Finally, the total FE towards liquid products is given in Figure 17. The electrolyte was analyzed after catalytic testing with NMR, which allowed us to measure the total FE. This value is used to determine the final total $FE_{missing}$, which is the current that has not been used for gaseous or liquid products. The products observed include formate, acetic acid, ethanol, and methanol. In the case of Cu-ref, the total $FE_{formate}$, $FE_{acetic\ acid}$, and $FE_{ethanol}$ are 5.3%, 6.6%, and 0.74%, respectively. This results in a total $FE_{missing}$ of 19%. Ag-ref exhibits a $FE_{formate}$ of 1.2% with a similar total $FE_{missing}$ of 19%. For Cu-Ag-gap, $FE_{formate}$, $FE_{acetic\ acid}$, and $FE_{methanol}$ are 7.5%, 0.36%, and 0.68%, respectively, resulting in a total $FE_{missing}$ of 19%. In the case of Cu-Ag-int, $FE_{formate}$, $FE_{methanol}$, $FE_{acetic\ acid}$, and $FE_{ethanol}$ are 10%, 0.36%, 0.68%, and 0.54%, respectively. This amounts to a total $FE_{missing}$ of 24%. For Cu-Ag-cod, $FE_{formate}$, $FE_{acetic\ acid}$, and $FE_{ethanol}$ are 6.0%, 1.1%, and 0.34%, respectively, resulting in a total $FE_{missing}$ of 17%. Finally, in the case of Cu-Ag-gr, $FE_{formate}$, $FE_{acetic\ acid}$, and $FE_{ethanol}$ are 5.0%, 0.20%, and 0.97%, respectively, leading to the lowest total $FE_{missing}$ of 11%. Because trace amounts of methanol and ethanol are observed, these products will be excluded from the discussion. The total $FE_{missing}$ can be explained by the leakage of electrolytes, currents, and gases. Another possibility is that the current has been utilized for metal reduction instead of the CO_2RR. The difference in total $FE_{missing}$ could be due to a human error in the manual assembly of the H-cell, resulting in variation of leaking. Subsequently, a brief elaboration on the product distribution and reaction pathways to the liquid products will be given.

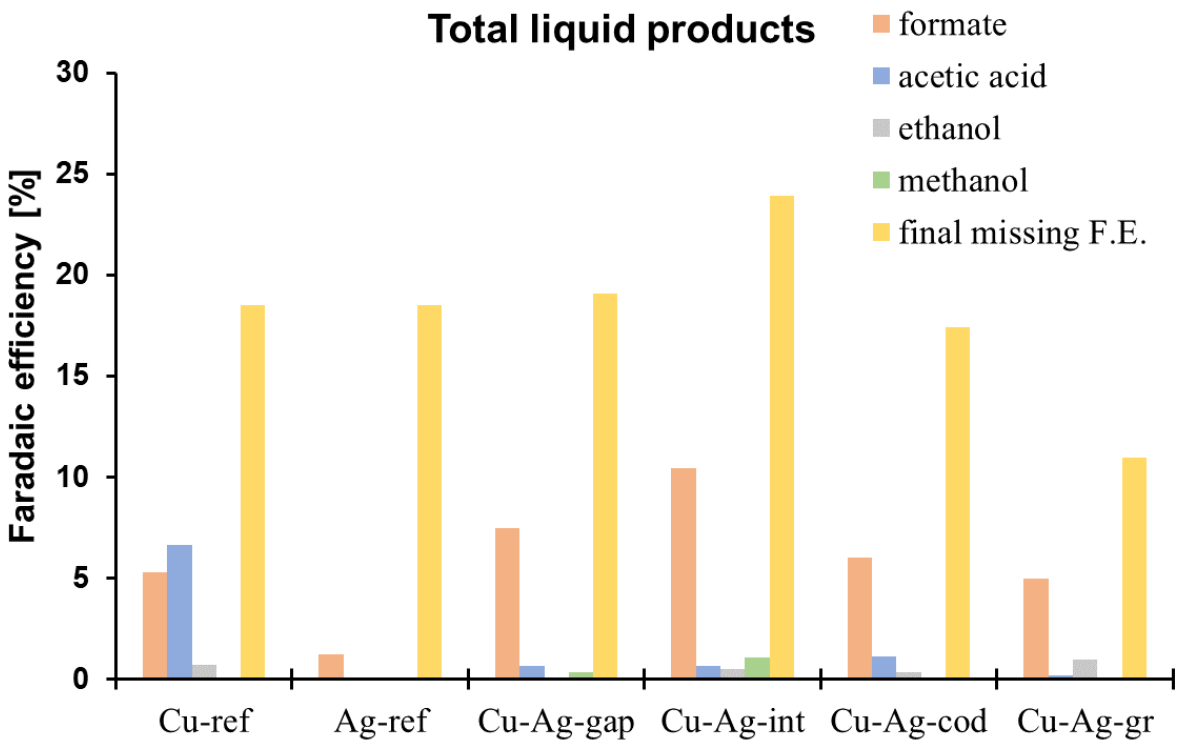

Figure 17. The total Faradaic efficiency to the liquid products including the total missing FE.

The production of formate (C_1) differs from other reaction pathways as it involves *OCHO as a key intermediate.[11] It is suggested that the reaction pathway to acetic acid (C_2) involves the protonation of the *CO intermediate following the same reaction pathway to methane/methanol[41] and that the reaction pathway to ethanol (C_2) involves *CO dimerization.[11,28] However, the exact mechanisms are not fully understood. Formate and both C_2 products can be produced by Cu-ref and only formate is produced by Ag-ref. For Cu-Ag-gap, $FE_{formate}$ increases while $FE_{acetic\ acid}$ decreases relative to Cu-ref. The promotion of formate is not fully understood, because it is expected to observe an increase in C_2 products when the abundance of *CO on the surface of Cu is increased through synergy. An explanation for the decline in $FE_{acetic\ acid}$ production could be that its reaction pathway, which is suggested to involve *CO protonation, is suppressed by the promotion of *CO dimerization. When the metals are interfaced, $FE_{formate}$ is increased compared to Cu-Ag-gap. Because the reaction pathway to formate involves the reduction of *OCHO, this observation is not understood. For Cu-Ag-cod, $FE_{acetic\ acid}$ is suppressed relative to Cu-ref, which could be attributed to the incorporation of Ag and/or the promotion of *CO dimerization. Finally, for Cu-Ag-gr nearly the same $FE_{formate}$ is observed as for Cu-ref, showing that Cu-ref still significantly contributes to the CO_2RR. Furthermore, the lowest $FE_{acetic\ acid}$ is observed, which could be related to the most effective synergy that promotes *CO dimerization and suppresses *CO protonation. The promotion of *CO dimerization is also observed by the highest $FE_{ethanol}$. Nevertheless, these correlations should be considered as presumptions, as proper analysis of possible reaction pathways to the liquid products should be provided, which goes beyond this study.

Based on the partial current densities, it can be concluded that Cu-Ag-int and Cu-Ag-cod exhibit the highest activity for ethylene production. Then, Cu-Ag-gr follows with a 70-fold increase in $j_{ethylene}$ compared to Cu-ref, which was used as the substrate for galvanic replacement. Involving the j_{CO} shows that Cu-Ag-gr exhibits lower activity for CO production compared to Cu-Ag-int and Cu-Ag-cod, suggesting that the majority of galvanically replaced Ag is involved in synergy. This property is characterized by $FE_{ethylene}>FE_{CO}$, resulting in the highest ethylene/CO ratio. Despite this, Cu-Ag-gr has the highest $j_{hydrogen}$, which can be attributed to the high activity of Cu-ref for the HER. To enhance the suppression of the HER, the time of galvanic replacement could be increased to deposit more Ag sites involved with galvanic replacement. In the following section, galvanic replacement is performed on uniform Cu_2O nanospheres, which have a higher catalytic surface area compared to Cu-ref. Furthermore, the uniformity of the particles can contribute to a better understanding of the effect of galvanic replacement.

4.3. Characterization of Cu_2O-Ag-*t* electrodes

The reference electrode was prepared by drop-casting copper(I)oxide nanospheres prepared via colloidal synthesis onto carbon paper. The galvanic replacement was performed using a 1 mM $AgNO_3$ solution for 1, 2, 3, and 4 minutes to prepare Cu_2O-Ag-0.5, Cu_2O-Ag-1, Cu_2O-Ag-2, and Cu_2O-Ag-4, respectively. To study the crystal structure, the XRD spectra were studied in the 2θ range from 40˚ to 80˚, as given in Figure 18. The XRD spectra are normalized to the highest intensity peak at 30.8˚, which is attributed to carbon paper. In Cu_2O-ref, the (111), (200), and (220) crystal planes of copper(I)oxide can be identified. For Cu_2O-Ag-0.5, the same crystal planes are detected with corresponding intensities. In the case of Cu_2O-Ag-1 and Cu_2O-Ag-2, an additional peak is observed at 50.8˚, which is attributed to Cu(111). After 4 minutes of galvanic replacement, Cu(111) can not be observed but an additional peak is observed at 44.6˚ corresponding to Ag(111).

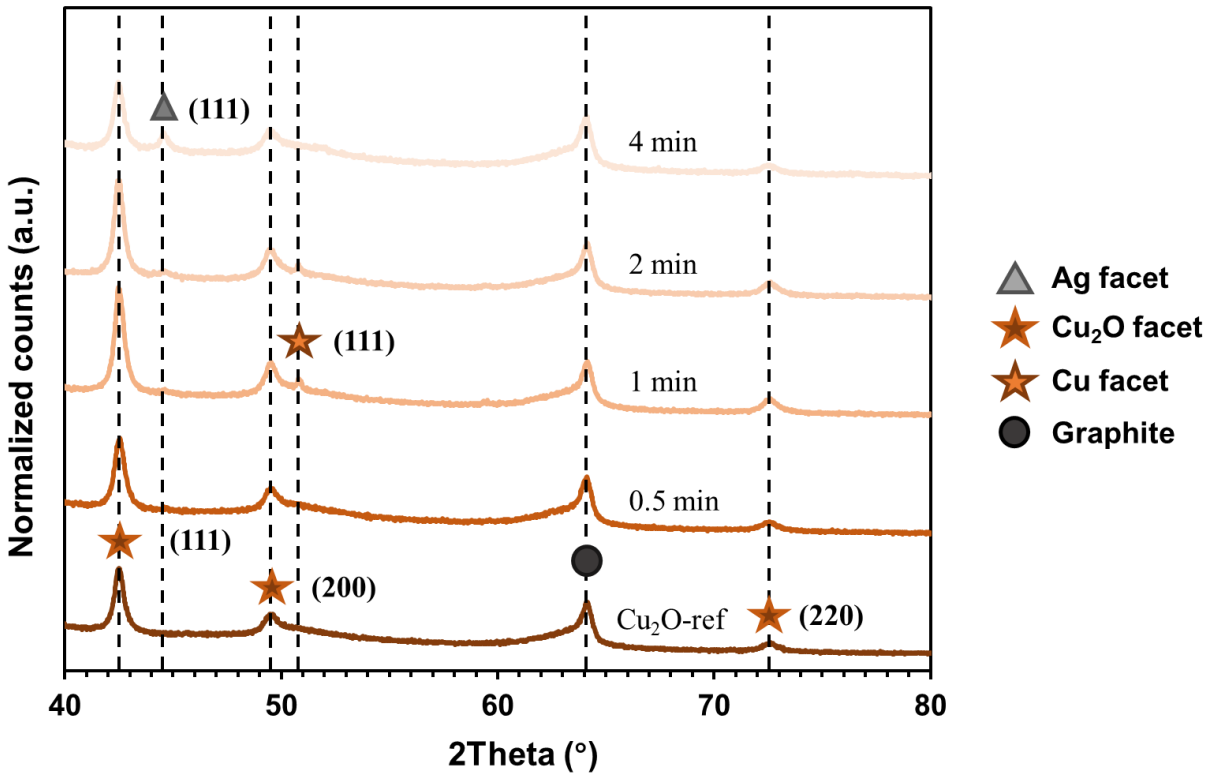

Figure 18. X-ray diffraction spectra in the 2θ range from 40˚ to 80˚ of the Cu_2O-Ag-*t* electrodes, where *t* corresponds to 0.5, 1, 2, or 4 minutes.

The crystal structure of the nanospheres is composed of non-preferential crystalline Cu_2O. It is expected that with increasing reaction time for galvanic replacement, more Ag will be deposited as a layer around Cu_2O-ref.[33] A similar spectrum is observed for Cu_2O-0.5 min as for the reference electrode, which can be explained by thin Ag deposits at the surface of Cu_2O-ref. Based on the broad and low-intensity peak of Cu-Ag-gr (Figure 7), it was suggested that galvanic replacement had primarily occurred at the surface of the substrate. To further elaborate on this, because the Ag deposit due to galvanic replacement is much thinner than the penetration depth of X-rays, detection can be very weak, and the peaks are not observed as they are lost in the

background noise.[38] After 1 minute of galvanic replacement, the Cu(111) crystal plane can be identified. With high-resolution SEM, the redeposition of Cu_2O was considered, which could be explained by the stable existence of Cu_2O species at neutral pH and an aerated environment. Since the bulk material is composed of Cu_2O-ref, it appears that it is likely that Cu^0 is redeposited. Another explanation for the detection of Cu could be that the reduction of Cu_2O before the galvanic replacement has led to the stable formation of Cu^0. However, this approach is less plausible because the Cu(111) peak is not identified in all electrodes. In the case of Cu_2O-Ag-2, the same crystal planes can be identified as for Cu_2O-Ag-1, including Cu(111). After 4 minutes of galvanic replacement, the Ag(111) crystal plane can be identified. This can be attributed to the formation of significantly large Ag crystals that can be detected by XRD. The absence of Cu(111) can be related to the relative long reaction time of galvanic replacement, which results in complete oxidation of redeposited Cu^0.

Subsequently, scanning electron microscopy was performed to study the relation between the crystal structure and the external shape of the deposited materials. Theoretically, 608 mg of Cu_2O nanospheres were deposited on the substrate, which is 1.85 times the mass of Cu (329 mg) deposited in Cu-ref. As given by the micrograph in Figure 19A, the Cu_2O nanospheres are evenly distributed onto the front carbon fibers of the carbon paper. The morphology appears less as a continuous film, but rather as individually deposited particles. Upon further magnification in Figure 19B, the colloidal particles are spherically shaped with an average size of 0.87 µm (σ = 0.061 µm), which was measured over the average diameter of 200 arbitrary particles (Figure A6 – Particle size distribution). Between the nanospheres, very few elongated particles can be observed due to the initiated growth of Cu nanowires. It can be assumed that these particles do not significantly contribute to the CO_2RR due to their low abundance. Subsequently, transmission electron microscopy was performed to study the surface of the Cu_2O nanosphere with higher resolution. The micrograph is given in Figure 19C and reveals that the nanosphere has a rough surface.

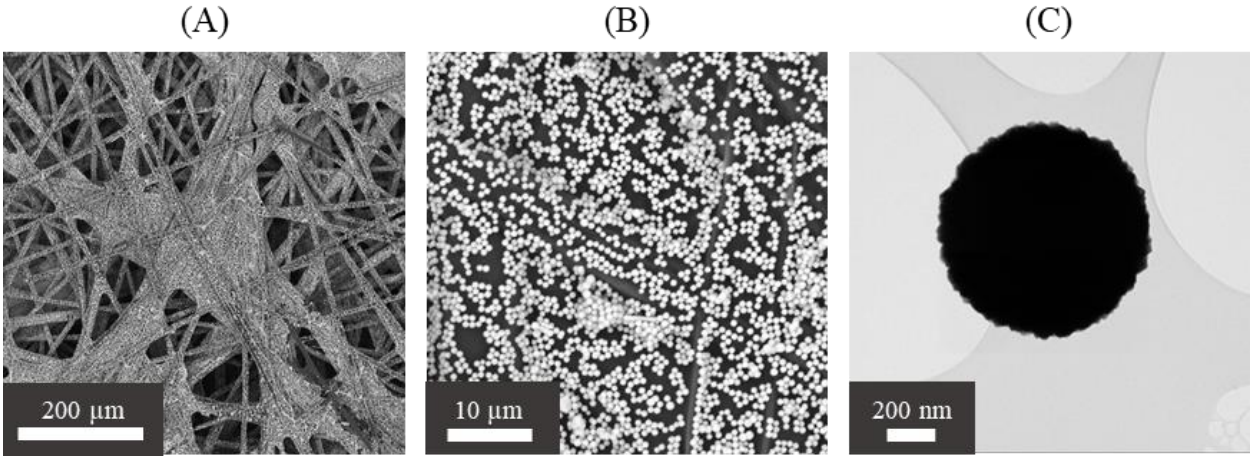

Figure 19. Micrographs obtained with SEM: (A) The coverage of carbon paper by drop casted Cu_2O nanospheres. (B) Uniform Cu_2O nanospheres prepared via colloidal synthesis. (C) TEM micrograph showing the rough surface of the nanosphere.

The effect of the time of the galvanic replacement using a 1 mM $AgNO_3$ solution on the morphology of the Cu_2O nanospheres is shown in Figure 20. For Cu_2O-Ag-0.5, the morphology of the nanospheres is preserved, and very small hairs emerge from the surface, which is likely galvanically replaced Ag. After 1 and 2 minutes, the morphology of the nanospheres is preserved, but the hairs emerging from the surface are larger. Crystalline Ag could not be detected by XRD at these times. Finally, after 4 minutes, the Ag(111) crystal plane could be identified in the XRD spectrum. This can be explained by the observation of larger Ag deposits covering the Cu_2O nanospheres in Figure 20D, which appear to be crystalline. Lastly, it was confirmed with SEM-EDX that the content of Ag on the surface increases with increasing reaction time. For 0.5, 1, 2, and 4 minutes, the Cu to Ag ratio was measured at 15.6, 10.8, 8.3, and 5.9, respectively [S9]. Subsequently, to evaluate the catalytic activity and selectivity of the CO_2RR, Cu_2O-ref, Cu_2O-Ag-1, and Cu_2O-Ag-4 are tested. This is done to obtain two catalysts that exhibit significantly different properties in the CO_2RR.

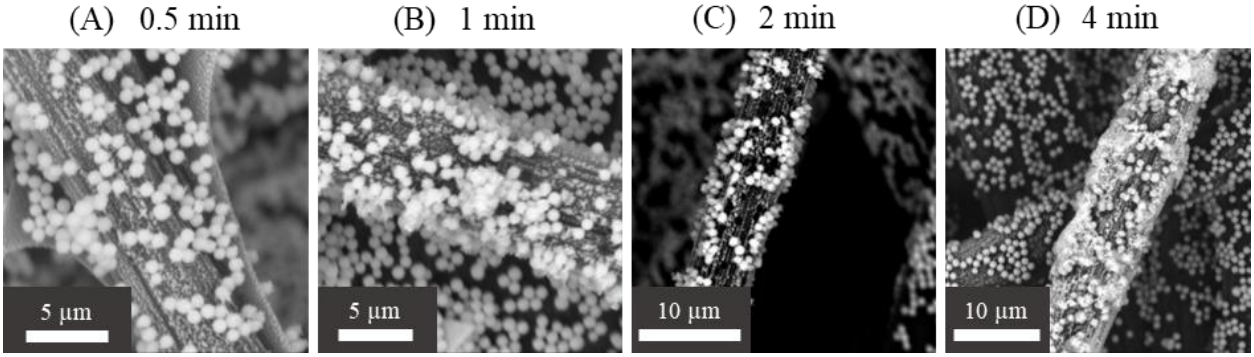

Figure 20. The effect of time of the galvanic replacement on the morphology of Cu_2O nanospheres using a 1 mM $AgNO_3$ solution.

4.4. Catalytic properties of Cu_2O-Ag-*t* nanosphere electrodes

Figure 21A displays the total current densities of Cu_2O-ref, Cu_2O-Ag-1, and Cu_2O-Ag-4. For comparison purposes, the current densities of Cu-ref and Cu-Ag-gr have also been added. It is important to mention that the current density of Cu_2O-ref is not measured at -1.4 V due to an overload error experienced by the potentiostat during catalytic testing. The higher j_{total} up to -1.2 V of Cu_2O-ref compared to Cu-ref is attributed to the increased surface area resulting from the deposition of Cu_2O nanospheres with approximately half the average size, but double the mass of Cu in Cu-ref. The j_{total} of Cu_2O-Ag-1 shows a decline at -1.2 V, followed by an increase at -1.4 V, which is also observed for Cu_2O-Ag-4. To elaborate further on trends found in j_{total}, the partial current densities for hydrogen, CO, and ethylene are given in Figures 21B-D. Methane or ethane production is not considered since only trace amounts were detected. Unfortunately, the product analysis on the GC experienced technical problems during catalytic testing of Cu_2O-Ag-4, by which the partial current densities could not be determined up to -1.2 V.

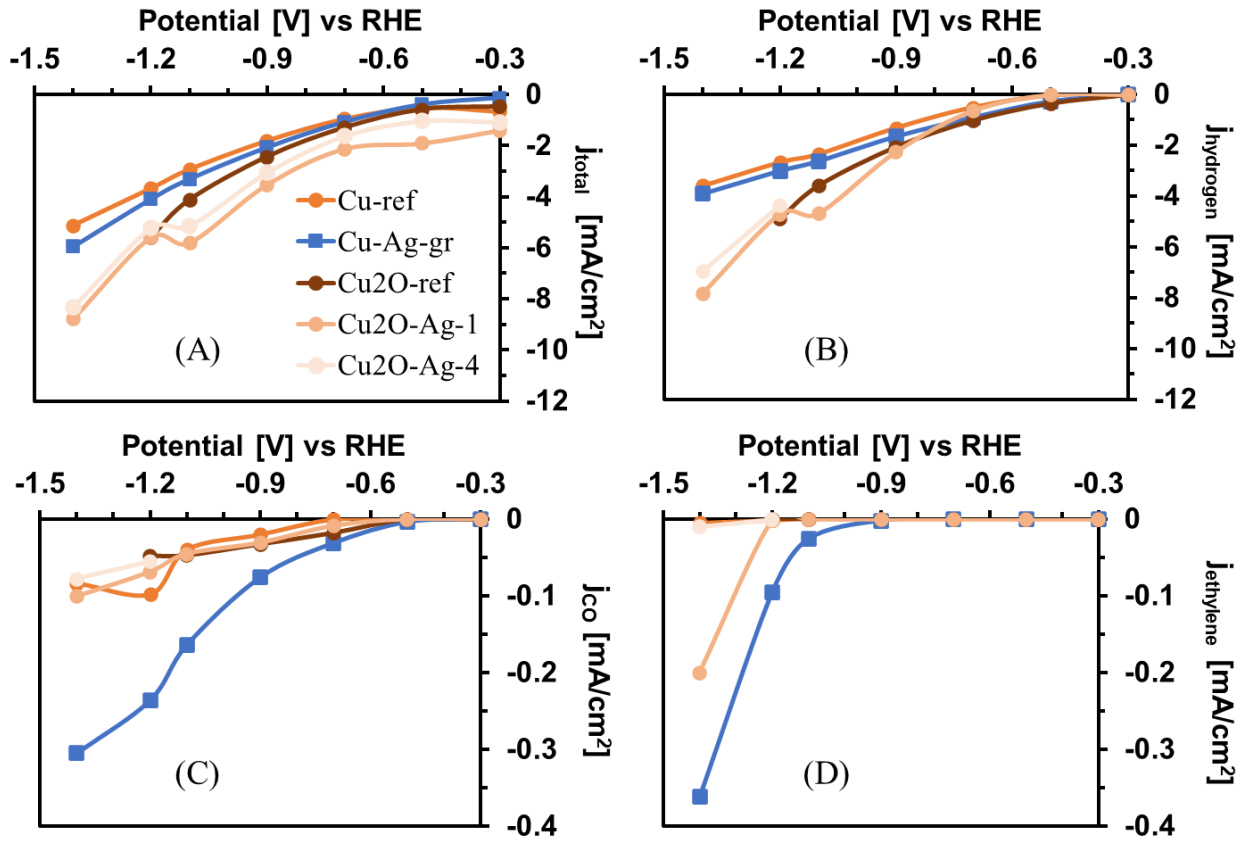

Figure 21. (A) The total current density and partial current densities to (B) hydrogen, (C) CO, and (D) ethylene of Cu_2O-ref, Cu_2O-Ag-1, and Cu_2O-Ag-4. Additionally, Cu-ref and Cu-Ag-gr are added for comparison.

Cu_2O-ref exhibits a higher $j_{hydrogen}$ compared to Cu-ref, which is explained by the poor activity of Cu for the CO_2RR. Consequently, increasing the catalytic surface area leads to a higher $j_{hydrogen}$, but should also lead to a higher j_{CO2RR}. Nevertheless, the j_{CO} of Cu_2O-ref is almost twice as low, while $j_{ethylene}$ is zero at -1.2 V. These observations might be the result of favored ethylene production at -1.4 V, as j_{CO} of Cu_2O-ref approaches a plateau at -1.2 V. However, considering the $j_{hydrogen}$ of Cu_2O-Ag-1 and Cu_2O-Ag-4, HER still accounts for most of the j_{total}, which was also observed for Cu-Ag-gr. Therefore, it can be concluded that the activity for the HER by Cu_2O-ref is not suppressed when the time of galvanic replacement is increased to 4 minutes. Furthermore, the j_{CO} increases with increasing potential and does not approach the plateau that was observed for Cu_2O-ref. This could indicate that primarily CO-producing Ag sites have been added to the catalysts by galvanic replacement. Presumably, this is the case for Cu_2O-Ag-4 because it exhibits a very low $j_{ethylene}$ and $FE_{ethylene}$ of 0.11%. This can be explained by the coverage of the Cu_2O nanospheres by Ag, which was observed with SEM in Figure 20D. The highest $j_{ethylene}$ of -0.20 mA/cm^2 is observed at -1.4 V for Cu_2O-Ag-1, which is 1.8-fold lower than the $j_{ethylene}$ of Cu-Ag-gr. However, due to the low j_{CO2RR} of Cu_2O-Ag-1, a $FE_{ethylene}$ of 2.3% was obtained, which is 2.6 times lower than was measured for Cu-Ag-gr. However, more effective synergy is observed in Cu_2O-Ag-1 based on its ethylene/CO ratio of 0.33.

Unfortunately, Cu_2O-Ag-0.5 and Cu_2O-Ag-2 have not been tested for CO_2RR due to time reasons. Nevertheless, it can be concluded that the attempt to enhance the partial current density and Faradaic efficiency of the CO_2RR towards ethylene through the modification of Cu_2O nanospheres with galvanic replacement has not been achieved after 1 or 4 minutes. This could be explained by that galvanic replacement has only modified a minority of the Cu_2O nanospheres on the front carbon fibers of the porous carbon paper, by which the poor activity of Cu_2O-ref for the CO_2RR is still strongly expressed. Consequently, increasing the time further does not affect more particles, but rather covers the particles on the front carbon fibers, resulting in reduced catalytic activity and selectivity towards ethylene. Therefore, it is suggested that a better understanding of the effect of time can be achieved by using a flat carbon substrate involving all the particles in the galvanic replacement. mitigating the poor activity of Cu.

Conclusion

This research has evaluated the catalytic activity and selectivity of the CO_2RR using Cu-Ag catalysts with different metal distributions to study the effectiveness of synergy. The synergistic effect is defined as the transfer of CO from Ag to Cu active sites, and increasing its effectiveness can steer the CO_2RR toward ethylene production. Electrodeposition was performed to prepare two electrodes with segregated phases of Cu and Ag that were separated or interfaced. The deposited materials were not preferentially oriented and exhibited spherical particle morphology. Additionally, co-deposition was performed to prepare Cu-Ag-cod representing particles with similar morphology and a homogeneous distribution of Cu and Ag. Lastly, Cu-Ag-gr was prepared by the immersion of a Cu substrate in a 1 mM $AgNO_3$ solution for 2 minutes, resulting in the deposition of a thin layer of Ag on top of the spherical Cu particles. Mostly the particles on the front carbon fibers of the carbon paper were affected by galvanic replacement.

Catalytic testing showed that interfacing Cu and Ag resulted in improved catalytic activity and selectivity towards ethylene compared to separated metals. The highest catalytic activity for ethylene production was obtained by the interface with $j_{ethylene}$ = -0.44 mA/cm^2 at -1.4 V vs RHE. The highest catalytic selectivity was achieved by a homogeneous distribution of Cu and Ag with a $FE_{ethylene}$ of 9.0%. However, to assess the effectiveness of the transfer of CO from Ag to Cu, the ethylene/CO ratio was considered. Despite not exhibiting the larger current density for ethylene nor the highest $FE_{ethylene}$, galvanic replacement resulted in the electrode with the highest ethylene/CO ratio of 0.18 at -1.4 V vs RHE. This shows that additional CO produced by deposited Ag is effectively transferred and utilized by Cu for further reduction into ethylene. The deposition of a thin layer of Ag via galvanic replacement led to a 70-fold increase in $j_{ethylene}$ to -0.36 mA/cm^2 and only a 3.6-fold increase in j_{CO} to -0.30 mA/cm^2 compared to the Cu substrate.

Subsequently, uniform Cu_2O nanospheres were synthesized via colloidal synthesis and drop-casted onto carbon paper. The galvanic replacement was performed with 1 mM $AgNO_3$ solution for 0.5, 1, 2, and 4 minutes. The Cu_2O nanospheres were non-preferentially oriented, exhibiting spherical morphology with an average size of 0.87 µm. It was shown that Cu_2O-Ag-1 and Cu_2O-Ag-4 exhibited worse activity and selectivity for CO_2RR towards ethylene compared to Cu-Ag-gr. However, the most effective synergy was observed in Cu_2O-Ag-1, considering the ethylene/CO ratio of 0.33 at -1.4 V vs RHE. It was shown with SEM that most Cu_2O nanospheres were unaffected by galvanic replacement due to the porous structure of carbon paper, by which the catalyst still exhibited the poor activity of the Cu_2O nanospheres for CO_2 reduction, favoring the HER.

In conclusion, tandem catalysis enables enhanced catalytic activity and selectivity towards ethylene in the CO_2RR by increasing the effectiveness of synergy. Interfacial contact of the metals is necessary to enhance the synergy between Cu and Ag. The homogeneous distribution of Cu and Ag resulted in the highest catalytic activity and selectivity towards ethylene and CO resulting in low effective synergy. Galvanic replacement is the most effective method for achieving effective synergy, but it is necessary to modify all the particles in the electrode to mitigate the poor activity of Cu in the CO_2RR.

Outlook

First, it is recommended that a flat substrate, such as glassy carbon, should be used to prepare Cu-Ag catalysts via galvanic replacement to modify all particles, mitigating the poor activity of Cu for CO_2 reduction. Additionally, to obtain better control of the galvanic replacement additives can be added. For instance, ligands and reducing agents can increase the homogeneity of galvanically replaced Ag and preserve the morphology of the Cu particles, respectively. This increases the reproducibility and comparability of the galvanic replacement with other Cu-Ag catalysts. Furthermore, more extensive analysis with high-resolution SEM can be performed to obtain a better understanding of the distribution of Cu and Ag due to galvanic replacement. In addition, inductive coupled plasma atomic emission spectroscopy or atomic adsorption spectroscopy can be performed to determine the real ratio between Cu and Ag in the catalysts.

In terms of catalytic testing, the cell resistance of the H-cell should be considered in follow-up research. It is important to correct for the cell resistance because the current density and Faradaic efficiency can be shifted in potential, which allows a more accurate comparison between the catalysts. In addition, Cu exhibits facet-dependent selectivity and other nanostructures can be explored to further enhance the production of ethylene in the CO_2RR.[42] For instance, a Cu nanowire primarily exposes the Cu(100) crystal plane that is more selective towards ethylene.[43,44] This facet-dependent selectivity makes these nanostructures more suitable for optimizing ethylene production compared to non-preferentially oriented Cu_2O nanospheres.

Finally, the time-dependent evolution of the catalytic activity and selectivity of Cu-based catalysts should be considered in the CO_2RR. Figure A7 presents the results of a 27-hour stability test for Cu-ref, which showed that the yield of hydrogen decreases, while the yield of CO and ethylene increases after approximately one hour. From this, it can be suggested that the surface of Cu was not saturated with CO_2RR intermediates within the first 30 minutes we measured for a potential.

Overall, while tandem catalysis has shown improvements in steering the CO_2RR towards ethylene, more research efforts must be taken to optimize the catalytic conversion of CO_2 into ethylene via effective synergy. By exploring cost-effective methods for preparing highly active and selective bulk catalysts towards the most valuable chemicals, the cost-efficiency and feasibility of the CO_2RR can be improved.

Acknowledgment

I would like to show my greatest thanks to Francesco Mattarozzi, who guided me with much interest through my master's thesis. I appreciate the feedback and help I received, and I am positively sure that I have learned a lot from working together. Additionally, I would like to thank the electrochemistry team for the interesting discussions that allowed me to take steps forwards in my project. I would like to thank Maaike van Ittersum and Claudia Keijzer for measuring high-resolution SEM, as well as Matt Peerlings for dedicating his time to measuring NMR. I would like to thank Prof. Dr. Petra De Jongh and Dr. Peter Ngene for the realization of my project and the feedback provided. Finally, I would like to thank all the researchers and staff members at MCC for creating a pleasant and meaningful time.

Bibliography

1. Holechek, J. L., Geli, H. M. E., Sawalhah, M. N. & Valdez, R. A Global Assessment: Can Renewable Energy Replace Fossil Fuels by 2050? *Sustain.* **14**, 1–22 (2022).
2. IPCC. *Global Warming of 1.5°C. An IPCC Special Report on the impacts of global warming of 1.5°C above pre-industrial levels and related global greenhouse gas emission pathways, in the context of strengthening the global response to the threat of climate change,*. (Cambridge University Press, 2018).
3. BP. BP Statistical Review of World Energy 2022,(71st edition). *Bp* 1–60 (2022).
4. Nitopi, S. *et al.* Progress and Perspectives of Electrochemical CO2 Reduction on Copper in Aqueous Electrolyte. *Chem. Rev.* **119**, 7610–7672 (2019).
5. Gür, T. M. Review of electrical energy storage technologies, materials and systems: Challenges and prospects for large-scale grid storage. *Energy Environ. Sci.* **11**, 2696–2767 (2018).
6. Wang, L. *et al.* Electrochemical Carbon Monoxide Reduction on Polycrystalline Copper: Effects of Potential, Pressure, and pH on Selectivity toward Multicarbon and Oxygenated Products. *ACS Catal.* **8**, 7445–7454 (2018).
7. De Luna, P. *et al.* What would it take for renewably powered electrosynthesis to displace petrochemical processes? *Science (80-.).* **364**, (2019).
8. Gao, Y. *et al.* Recent Advances in Intensified Ethylene Production - A Review. *ACS Catal.* **9**, 8592–8621 (2019).
9. Hori, Y., Murata, A. & Takahashi, R. Formation of hydrocarbons in the electrochemical reduction of carbon dioxide at a copper electrode in aqueous solution. *J. Chem. Soc. Faraday Trans. 1 Phys. Chem. Condens. Phases* **85**, 2309–2326 (1989).
10. Bagger, A., Ju, W., Varela, A. S., Strasser, P. & Rossmeisl, J. Electrochemical CO2 Reduction: A Classification Problem. *ChemPhysChem* **18**, 3266–3273 (2017).
11. Kortlever, R., Shen, J., Schouten, K. J. P., Calle-Vallejo, F. & Koper, M. T. M. Catalysts and Reaction Pathways for the Electrochemical Reduction of Carbon Dioxide. *J. Phys. Chem. Lett.* **6**, 4073–4082 (2015).
12. Sandberg, R. B., Montoya, J. H., Chan, K. & Nørskov, J. K. CO-CO coupling on Cu facets: Coverage, strain and field effects. *Surf. Sci.* **654**, 56–62 (2016).
13. Zhang, W. *et al.* Atypical Oxygen-Bearing Copper Boosts Ethylene Selectivity toward Electrocatalytic CO2Reduction. *J. Am. Chem. Soc.* **142**, 11417–11427 (2020).
14. Gao, D. *et al.* Selective CO2 Electroreduction to Ethylene and Multicarbon Alcohols via Electrolyte-Driven Nanostructuring. *Angew. Chemie - Int. Ed.* **58**, 17047–17053 (2019).
15. Huang, Y., Ong, C. W. & Yeo, B. S. Effects of Electrolyte Anions on the Reduction of Carbon Dioxide to Ethylene and Ethanol on Copper (100) and (111) Surfaces. *ChemSusChem* **11**, 3299–3306 (2018).

16. Li, F. *et al.* Molecular tuning of CO2-to-ethylene conversion. *Nature* **577**, 509–513 (2020).

17. Huang, J., Mensi, M., Oveisi, E., Mantella, V. & Buonsanti, R. Structural Sensitivities in Bimetallic Catalysts for Electrochemical CO2 Reduction Revealed by Ag-Cu Nanodimers. *J. Am. Chem. Soc.* **141**, 2490–2499 (2019).

18. Chen, C. *et al.* Cu-Ag Tandem Catalysts for High-Rate CO2 Electrolysis toward Multicarbons. *Joule* **4**, 1688–1699 (2020).

19. da Silva, A. H. M. *et al.* Electrocatalytic CO2 reduction to C2+ products on Cu and CuxZny electrodes: Effects of chemical composition and surface morphology. *J. Electroanal. Chem.* **880**, (2021).

20. Cuya Huaman, J. L., Urushizaki, I. & Jeyadevan, B. Large-scale Cu nanowire synthesis by PVP-ethylene glycol route. *J. Nanomater.* **2018**, (2018).

21. Gamburg, Y. D. & Zangari, G. Equilibrium Potential and Overpotential. in *Theory and Practice of Metal Electrodeposition* 8–9 (Springer Science+Business Media, LCC, 2011).

22. Xing, Z., Hu, L., Ripatti, D. S., Hu, X. & Feng, X. Enhancing carbon dioxide gas-diffusion electrolysis by creating a hydrophobic catalyst microenvironment. *Nat. Commun.* **12**, 1–11 (2021).

23. Chang, F. *et al. Copper-Based Catalysts for Electrochemical Carbon Dioxide Reduction to Multicarbon Products*. *Electrochemical Energy Reviews* vol. 5 (Springer Nature Singapore, 2022).

24. Miles, M. H. *et al.* The oxygen evolution reaction on platinum, iridium, ruthenium and their alloys at 80°C in acid solutions. *Electrochim. Acta* **23**, 521–526 (1978).

25. Ren, D., Ang, B. S. H. & Yeo, B. S. Tuning the Selectivity of Carbon Dioxide Electroreduction toward Ethanol on Oxide-Derived CuxZn Catalysts. *ACS Catal.* **6**, 8239–8247 (2016).

26. Cook, R. L., MacDuff, R. C. & Sammells, A. F. Evidence for Formaldehyde, Formic Acid, and Acetaldehyde as Possible Intermediates during Electrochemical Carbon Dioxide Reduction at Copper. *J. Electrochem. Soc.* **136**, (1989).

27. Zhang, H., Liu, X., Li, H., Hasa, I. & Passerini, S. Challenges and Strategies for High-Energy Aqueous Electrolyte Rechargeable Batteries. *Angew. Chemie - Int. Ed.* **60**, 598–616 (2021).

28. Pan, F. & Yang, Y. Designing CO2reduction electrode materials by morphology and interface engineering. *Energy Environ. Sci.* **13**, 2275–2309 (2020).

29. Yang, Y., Tan, Z. & Zhang, J. Electrocatalytic Carbon Dioxide Reduction to Ethylene over Copper-based Catalytic Systems. *Chem. - An Asian J.* **17**, (2022).

30. Feng, Y. *et al.* Laser-Prepared CuZn Alloy Catalyst for Selective Electrochemical Reduction of CO2 to Ethylene. *Langmuir* **34**, 13544–13549 (2018).

31. De Oliveira, G. M. & Carlos, I. A. Silver-copper electrodeposition from ammonium

hydroxide solution: Influence of EDTA and HEDTA. *J. Appl. Electrochem.* **39**, 1217–1227 (2009).

32. Jeon, Y., Choe, S., Kim, H. C., Kim, M. J. & Kim, J. J. Electrodeposition of Cu-Ag films in ammonia-based electrolyte. *J. Alloys Compd.* **775**, 639–646 (2019).

33. Papaderakis, A., Mintsouli, I., Georgieva, J. & Sotiropoulos, S. Electrocatalysts prepared by galvanic replacement. *Catalysts* **7**, (2017).

34. Jing, H. & Wang, H. Structural evolution of Ag-Pd bimetallic nanoparticles through controlled galvanic replacement: Effects of mild reducing agents. *Chem. Mater.* **27**, 2172–2180 (2015).

35. Zhang, Y. *et al.* PVP-Mediated Galvanic Replacement Synthesis of Smart Elliptic Cu-Ag Nanoflakes for Electrically Conductive Pastes. *ACS Appl. Mater. Interfaces* **11**, 8382–8390 (2019).

36. Sakai, K., Iwamura, S., Sumida, R., Ogino, I. & Mukai, S. R. Carbon paper with a high surface area prepared from carbon nanofibers obtained through the liquid pulse injection technique. *ACS Omega* **3**, 691–697 (2018).

37. Sen, P., Ghosh, J., Abdullah, A., Kumar, P. & Vandana. Preparation of Cu, Ag, Fe and Al nanoparticles by the exploding wire technique. *Proc. Indian Acad. Sci. Chem. Sci.* **115**, 499–508 (2003).

38. Harrington, G. F. & Santiso, J. Back-to-Basics tutorial: X-ray diffraction of thin films. *J. Electroceramics* **47**, 141–163 (2021).

39. Celante, V. G. & Freitas, M. B. J. G. Electrodeposition of copper from spent Li-ion batteries by electrochemical quartz crystal microbalance and impedance spectroscopy techniques. *J. Appl. Electrochem.* **40**, 233–239 (2010).

40. Inzelt, G. *Encyclopedia of Applied Electrochemistry*. *Encyclopedia of Applied Electrochemistry* (2014). doi:10.1007/978-1-4419-6996-5.

41. Genovese, C., Ampelli, C., Perathoner, S. & Centi, G. Mechanism of C-C bond formation in the electrocatalytic reduction of CO2 to acetic acid. A challenging reaction to use renewable energy with chemistry. *Green Chem.* **19**, 2406–2415 (2017).

42. De Gregorio, G. L. *et al.* Facet-Dependent Selectivity of Cu Catalysts in Electrochemical CO2 Reduction at Commercially Viable Current Densities. *ACS Catal.* **10**, 4854–4862 (2020).

43. Choi, C. *et al.* Intimate atomic Cu-Ag interfaces for high CO2RR selectivity towards CH4 at low over potential. *Nano Res.* **14**, 3497–3501 (2021).

44. Ni, B. & Wang, X. Face the Edges: Catalytic Active Sites of Nanomaterials. *Adv. Sci.* **2**, 1–22 (2015).

Appendix

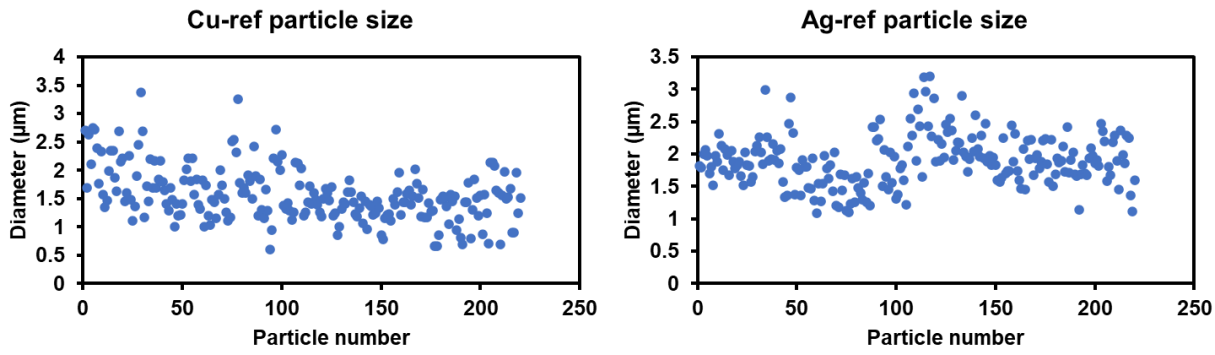

Figure A1. Particle size distribution of Cu-ref and Ag-ref.

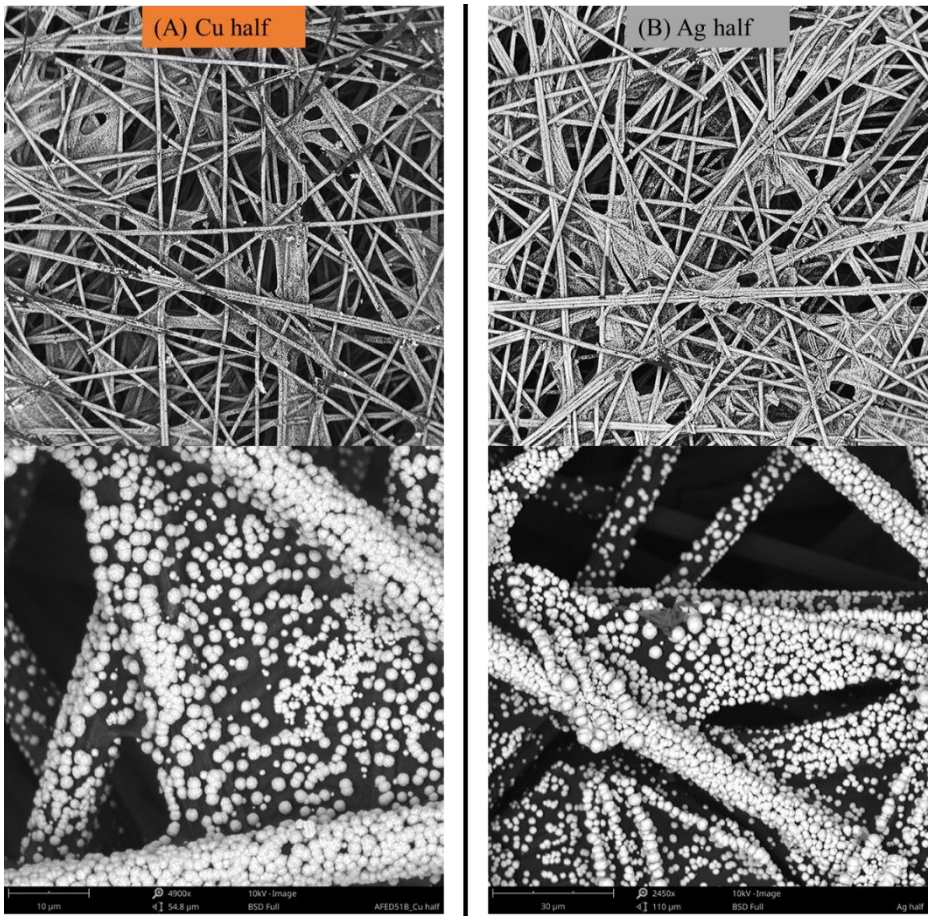

Figure A2. The coverage of carbon paper and particle morphology of the Cu and Ag half in Cu-Ag-gap.

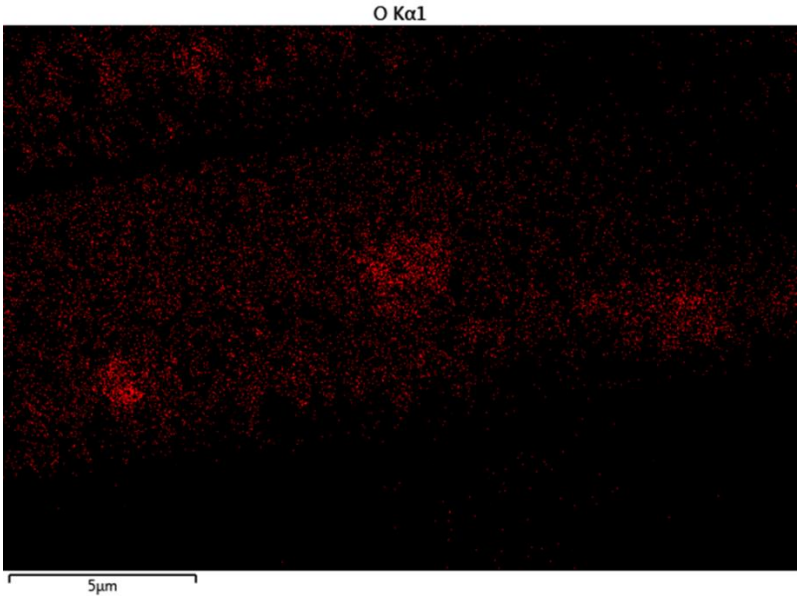

Figure A3. Detection of surface oxygen in Cu-Ag-cod.

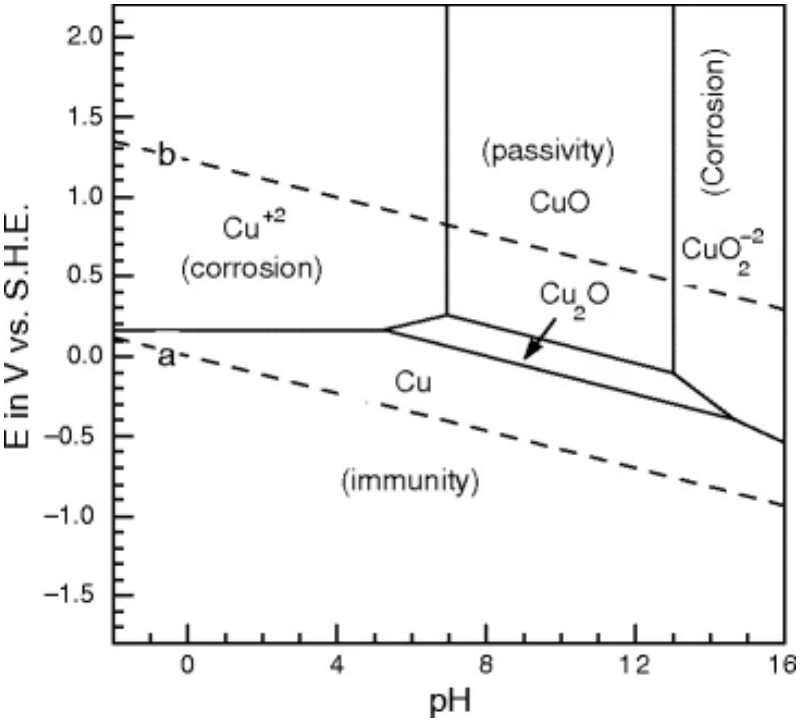

Figure A4. Pourbaix diagram of copper in an aqueous environment.

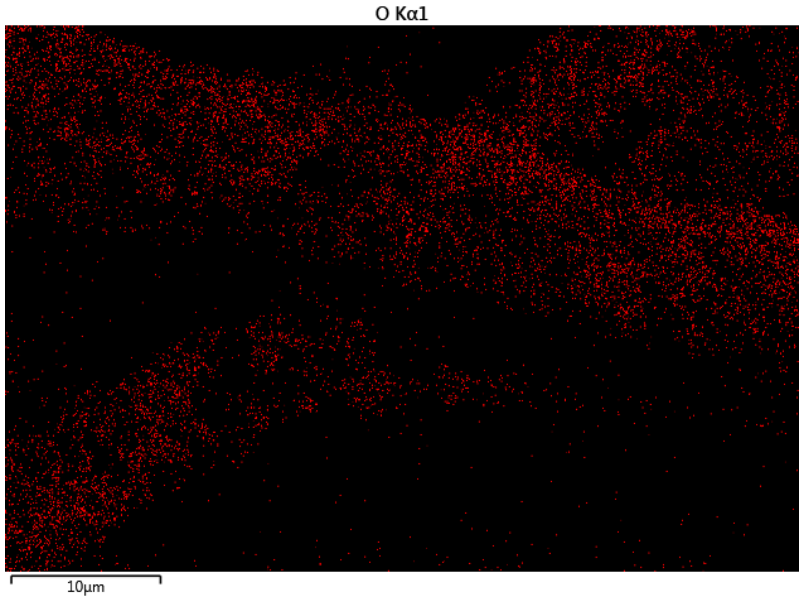

Figure A5. Detection of surface oxygen in Cu-Ag-gr.

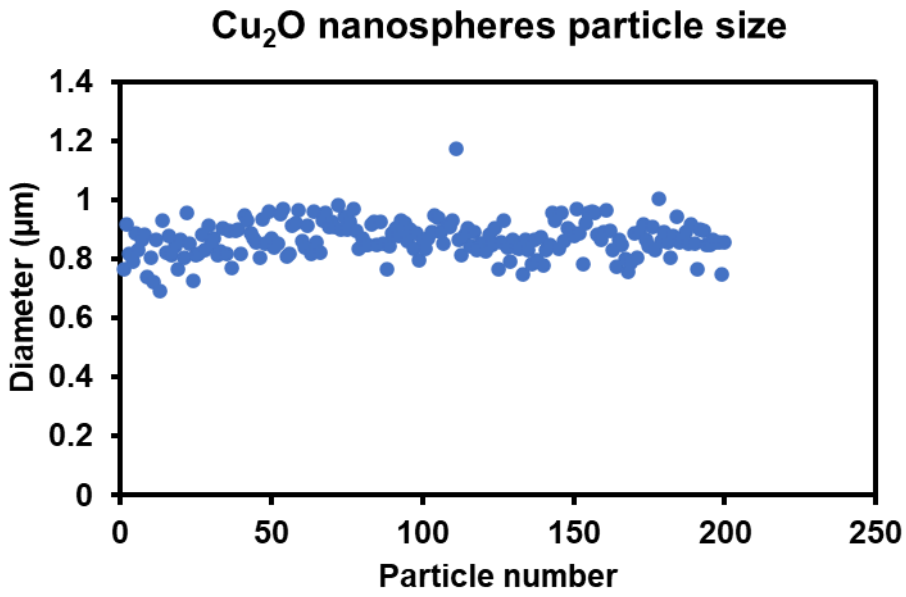

Figure A6. Particle size distribution of Cu_2O nanospheres.

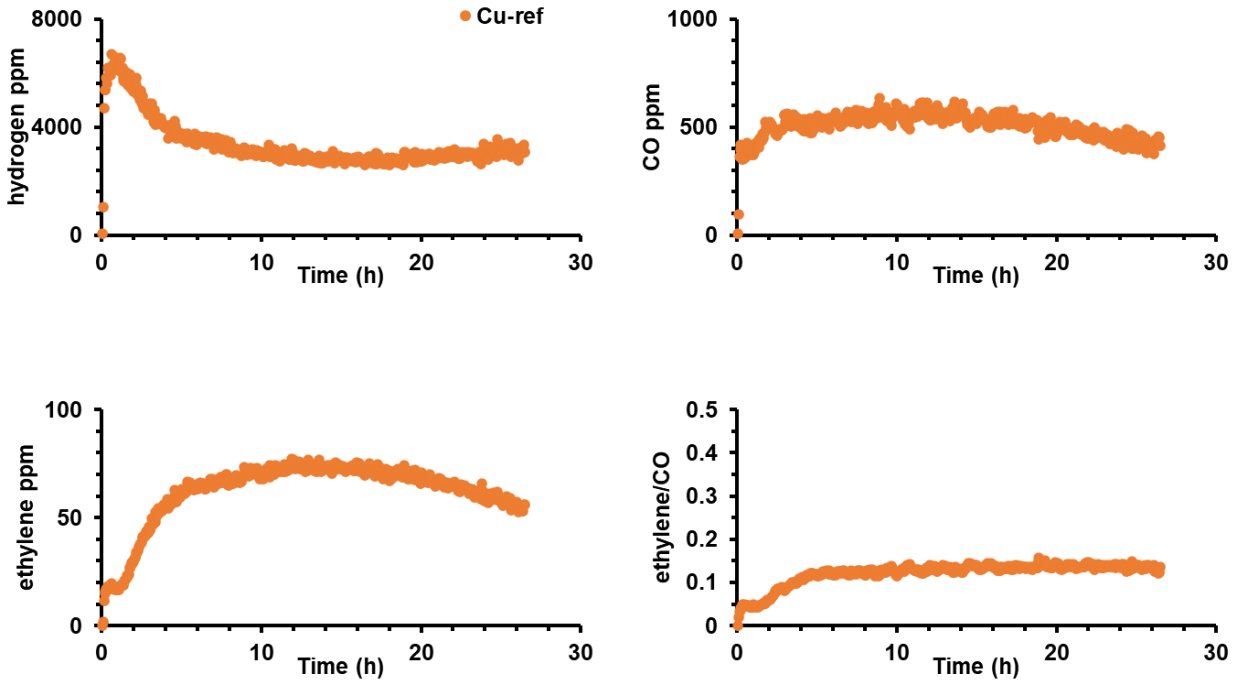

Figure A7. Evolution of hydrogen, CO, and ethylene yield in ppm, including ethylene/CO ratio as a function of time.